J. Fluid Mech. (1996), *vol.* 314, *pp.* 373–405

An experimental study of absolute instability of the rotating-disk boundary-layer flow

By R. J. LINGWOOD

Department of Engineering, University of Cambridge, Trumpington Street, Cambridge CB2 1PZ, UK

(Received 29 September 1995 and in revised form 25 January 1996)

In this paper, the results of experiments on unsteady disturbances in the boundary-layer flow over a disk rotating in otherwise still air are presented. The flow was perturbed impulsively at a point corresponding to a Reynolds number R below the value at which transition from laminar to turbulent flow is observed. Among the frequencies excited are convectively unstable modes, which form a three-dimensional wave packet that initially convects away from the source. The wave packet consists of two families of travelling convectively unstable waves that propagate together as one packet. These two families are predicted by linear-stability theory: branch-2 modes dominate close to the source but, as the packet moves outwards into regions with higher Reynolds numbers, branch-1 modes grow preferentially and this behaviour was found in the experiment. However, the radial propagation of the trailing edge of the wave packet was observed to tend towards zero as it approaches the critical Reynolds number (about 510) for the onset of radial absolute instability. The wave packet remains convectively unstable in the circumferential direction up to this critical Reynolds number, but it is suggested that the accumulation of energy at a well-defined radius, due to the flow becoming radially absolutely unstable, causes the onset of laminar–turbulent transition. The onset of transition has been consistently observed by previous authors at an average value of 513, with only a small scatter around this value. Here, transition is also observed at about this average value, with and without artificial excitation of the boundary layer. This lack of sensitivity to the exact form of the disturbance environment is characteristic of an absolutely unstable flow, because absolute growth of disturbances can start from either noise or artificial sources to reach the same final state, which is determined by nonlinear effects.

1. Introduction

This paper presents results from an experimental study of the stability of the laminar boundary-layer flow over a rotating disk. The rotating-disk boundary layer is similar to that over a swept wing; both boundary layers are three-dimensional with a laminar velocity component that is inflectional. Hence, both flows are susceptible to inviscid crossflow instability. This form of instability was first noticed experimentally by Gray (1952) in the flow over a swept wing. His visualization experiments showed that transition occurs at much lower Reynolds numbers on swept wings than unswept wings and that, before transition, the surface of the wing is covered with a stationary striped pattern lying in the streamwise direction, which was explained as a series of stationary vortices in the boundary layer. The classic paper by Gregory, Stuart

& Walker (1955), on three-dimensional boundary-layer stability, and the earlier hot-wire anemometry investigation by Smith (1946) showed the same behaviour in the rotating-disk boundary layer. Since the work by Gregory *et al.* (1955), the rotating disk has been used extensively as a model for the boundary layer on a swept wing. The rotating-disk problem has certain advantages and simplifications over the swept-wing problem: the rotating-disk flow does not have a pressure-gradient parameter or a variable sweep angle, it has good experimental control and there is an exact similarity solution of the Navier–Stokes equations for the base flow, in which the shape of the laminar velocity profiles is independent of the radius. The boundary-layer thickness is also independent of the radius.

It was suggested by Gregory *et al.* (1955) that small roughness elements on the surface fix the vortex pattern in the rotating-disk boundary layer relative to the surface. This conjecture was strengthened by the experimental study by Wilkinson & Malik (1985) and the theoretical work by Mack (1985). The agreement between these two studies showed that the stationary vortices are the result of interfering wave patterns originating from randomly positioned roughnesses on the surface of the disk. Between 28 and 32 vortices, with a wave angle of about 14° to the outward radius vector in the direction of rotation, are observed (e.g. Gregory *et al.* 1955) once the individual patterns have merged and filled the whole circumference of the disk. By analysing the frequency content of the noise generated within the boundary layer, Gregory *et al.* (1955) concluded that there are travelling waves as well as stationary waves, but naturally their china-clay visualization experiments indicated only disturbances fixed relative to the disk. Because of such visualization experiments, with few exceptions (e.g. Bassom & Gajjar 1988; Wilkinson *et al.* 1989; Balakumar & Malik 1990; Bassom & Hall 1991; Faller 1991), previous studies of the rotating-disk boundary layer have concentrated on the stationary waves. However, the boundary layer is also susceptible to excitation from free-stream turbulence and some of the resulting travelling waves are more unstable than the stationary waves.

The stationary vortices, which using the terminology of Lingwood (1995*a*) are the zero-frequency subset of the 'branch-1' modes (a branch of the dispersion relation that is unstable in the inviscid limit), are usually observed in experiments. However, Fedorov *et al.* (1976) observed a mode, using visualization techniques, that had a wave angle of about 20° and gave between 14 and 16 vortices around the disk. These experimental results represent one of few observations of 'branch-2' vortices (a branch of the dispersion relation that is stable in the inviscid limit). Figure 6 of Lingwood (1995*a*) gives a selection of neutral-stability curves (for stationary and travelling waves) that shows branches 1 and 2. The nonlinear asymptotic analysis by MacKerrell (1987) suggests that stationary branch-2 vortices are dominant for large-amplitude disturbances but the normally observed branch-1 vortices dominate for small-amplitude disturbances. This suggestion is supported by the theoretical and experimental work of Faller (1991).

Malik, Wilkinson & Orszag (1981) tabulated locations for the onset of transition, as found by various experimentalists, and the values show a scatter of less than 3% around an average Reynolds number of 513, despite various methods of investigation. In particular, experiments by Chin & Litt (1972) showed a well-defined transition Reynolds number of 510 and the early experiments of Theodorsen & Regier (1945) showed that the Reynolds number for the onset of transition, derived from measurements of the local drag coefficient, occurred abruptly at $R \approx 510$ and could not be increased whatever precautions were taken to make the disk smoother. These results are in sharp contrast with the onset of transition of the boundary-layer flow on, say,

a flat plate, where the onset is sudden but the location is highly dependent on the disturbance environment. These observations led M. Gaster (1992, personal communication) to suggest the possibility that a well-defined location of absolute instability of the rotating-disk boundary layer may be triggering the nonlinear behaviour characteristic of the onset of transition. Note that some researchers have obtained higher transition Reynolds numbers for the rotating-disk flow, e.g. Wilkinson & Malik (1985) give values of 543–556 for a 'clean' disk and 521–530 for a disk with an artificial roughness element. This difference is because they used different criteria for judging when the flow is transitional.

In a previous paper (Lingwood 1995*a*) results were presented from a linear-stability analysis of the rotating-disk boundary-layer flow, which considers travelling waves (non-zero frequency) as well as stationary waves. The viscous analysis, which assumes that the flow is locally parallel (i.e. that locally there is no variation in Reynolds number with radius), includes streamline-curvature and Coriolis effects, and shows that for $R > 510.625$ the flow becomes radially absolutely unstable, meaning that disturbances grow temporally at fixed radii, leading to an unbounded linear response that will promote nonlinearity and maybe transition. Below this Reynolds number the flow is convectively unstable or stable depending on the parameter values. Lingwood (1995*a*) uses Briggs' method (Briggs 1964) to distinguish between convectively and absolutely unstable time-asymptotic responses to impulsive forcing. The absolute instability is shown to result from a coalescence, or 'pinching', of two branches of the dispersion relation at a complex frequency with non-zero real part and, importantly, with imaginary part indicating temporal growth. From Briggs' criterion for absolute instability, these two modes necessarily represent waves that propagate away from the source in opposite directions. The two modes involved are branches 1 and 3, where branch-3 modes propagate energy inwards (towards the centre of the disk) but are always spatially damped and therefore do not appear on neutral-stability curves for convective instability such as figure 6 of Lingwood (1995*a*). Except for Mack (1985) and Balakumar & Malik (1990), branch-3 modes are not mentioned in the literature, probably because the rotating-disk problem was thought to be at most convectively unstable and, with this erroneous assumption, branch-3 modes were not considered to be any more important than other convectively damped modes.

If the linear response to a transient disturbance, e.g. the impulse response, is unbounded for large time at all points in space, the flow is said to be absolutely unstable, although in a physical system the amplitude of any disturbance is limited by nonlinear effects. Sketches of typical impulse responses are shown in figure 1, where the radius is r, the radial location of the source of the impulse is given by r_s and disturbances are exponentially amplified within the dashed lines. Figure 1 (*a*) shows a convectively unstable case, figure 1 (*b*) shows an absolutely unstable case and figure 1 (*c*) shows a flow that changes from being convectively to absolutely unstable as the Reynolds number (defined as $R = r(\Omega/\nu)^{1/2}$, where Ω is the rotation speed and ν is the kinematic viscosity of air), increases with r, i.e. in a non-parallel flow. In the convectively unstable case, in figure 1 (*a*), the disturbance propagates away from the source as it grows, leaving the source area undisturbed. In contrast, for the absolutely unstable case, in figure 1 (*b*), the response spreads into regions on both sides of the source, so that the disturbance grows in time at fixed radial positions. In figure 1 (*c*) the source of the disturbance lies in the convectively unstable region of the flow and so the disturbance initially propagates away, but at a certain Reynolds number, or

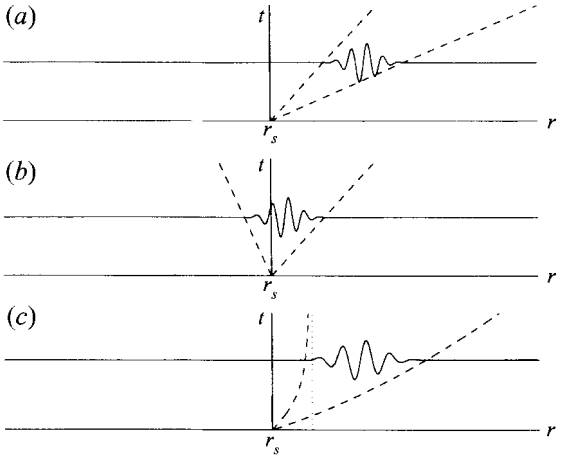

FIGURE 1. Sketches of space-time diagrams for typical impulse responses: (*a*) convectively unstable, (*b*) absolutely unstable, (*c*) initially convectively unstable but becoming absolutely unstable at Reynolds numbers corresponding to radii to the right of the vertical dotted line. The wave packets between the dashed lines represent the extent of the unstable region.

radius, the flow becomes absolutely unstable and the trailing edge of the wedge of instability asymptotes towards the vertical, which implies that beyond this radius the disturbance grows in time at all fixed radial positions.

In the experimental study by Wilkinson & Malik (1985), an artificial roughness element was placed on the surface of the disk; this created larger than normal disturbances, which were easier to measure with a hot-wire anemometer. A variant on this idea has been used in the experimental study of the rotating-disk boundary layer presented in this paper. Instead of an artificial roughness, a deterministic impulsive disturbance has been used to artificially excite the boundary layer with a broad frequency spectrum. Through selective amplification of the unstable modes, this procedure allows reproducible travelling waves to be measured, as well as the stationary waves originating from unavoidable roughnesses on the surface. In a similar manner to Wilkinson & Malik (1985), a hot-wire probe was used to measure the flow. Although this is an invasive technique, which will cause some disturbance to the flow field, it is hoped that this disturbance is small. Furthermore, where the flow is convectively unstable, all growing disturbances are swept outwards, which means that it is unlikely that the hot wire measures disturbances that it created itself on previous rotations of the disk.

It should be noted that if there are large roughness elements on the surface of the disk, stationary vortices may grow sufficiently to distort the mean velocity profiles, causing secondary instabilities (Kobayashi, Kohama & Takamadate 1980; Kohama 1984, 1987; Balachandar, Streett & Malik 1990). Based on smoke-visualization experiments, Kohama (1984) suggested that the secondary instability takes the form of ring-like co-rotating vortices that appear on the surface of each stationary vortex. The Floquet analysis performed by Balachandar *et al.* (1990) showed that, unlike a two-dimensional boundary layer, secondary instability in a crossflow dominated three-dimensional boundary layer occurs only under significant modulation of the mean flow (two orders of magnitude greater than for a two-dimensional boundary layer). It was assumed in the theoretical analysis presented in Lingwood (1995*a*), for absolute instability, that wall-roughness and free-stream-turbulence levels are both

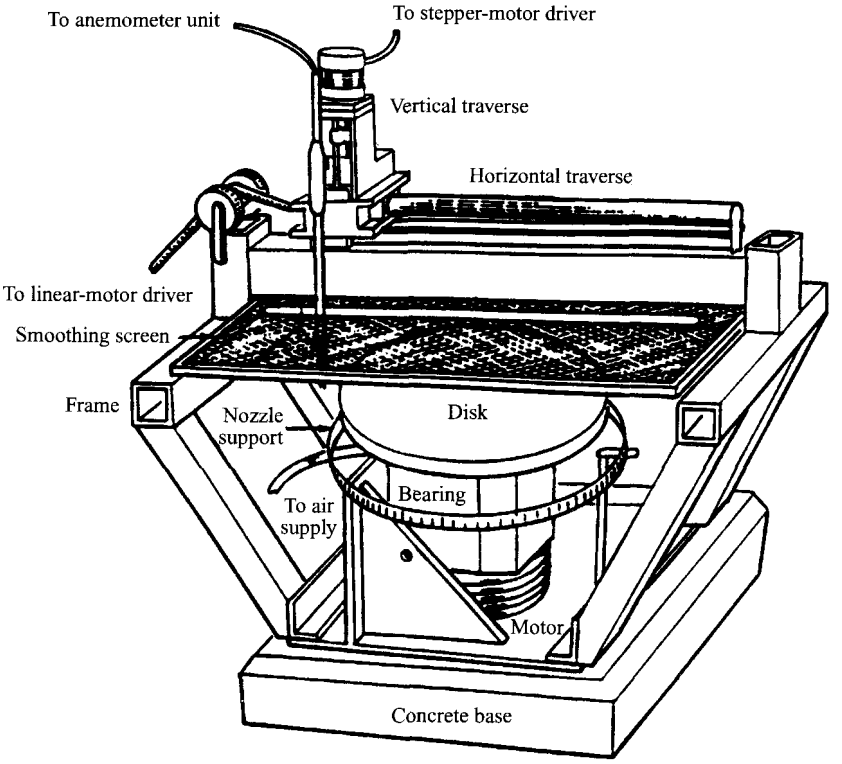

FIGURE 2. A sketch of the experimental rig.

sufficiently small for the transition process to be controlled by the stability of the mean velocity profiles rather than secondary instabilities, i.e. the model assumes a sufficiently 'clean' environment. To enable comparison with the earlier theoretical results, the experimental study described here was performed in as clean an environment as possible. Therefore, it is possible that in a less clean environment the dominant transition mechanisms is not radial absolute instability, as proposed here, but a secondary instability of the modulated base flow.

The experimental apparatus is described in §2 and was designed and built for this investigation. The aim was to minimize, as far as possible, surface roughness and vibration of disk as it rotates. Measurements of the mean velocity profiles are given in §3.1. Details of the 'unexcited' boundary-layer behaviour, i.e. the behaviour without any artificial excitation of the boundary layer but nonetheless excited by unavoidable sources, are given in §3.2. In the main part of the investigation the boundary layer was excited impulsively at a point and the development of the resulting three-dimensional wave packet has been measured and the results are presented in §3.3. It is shown that the flow tends towards absolute instability as the Reynolds number predicted by the theoretical study (Lingwood 1995*a*) is approached.

2. Experimental arrangement

Measurements were conducted with the rotating disk sketched in figure 2. It consists of a 475 mm diameter, 30 mm deep, stabilized aluminium-alloy disk that was finished with a single-crystal diamond cutting tool to near optical quality. The

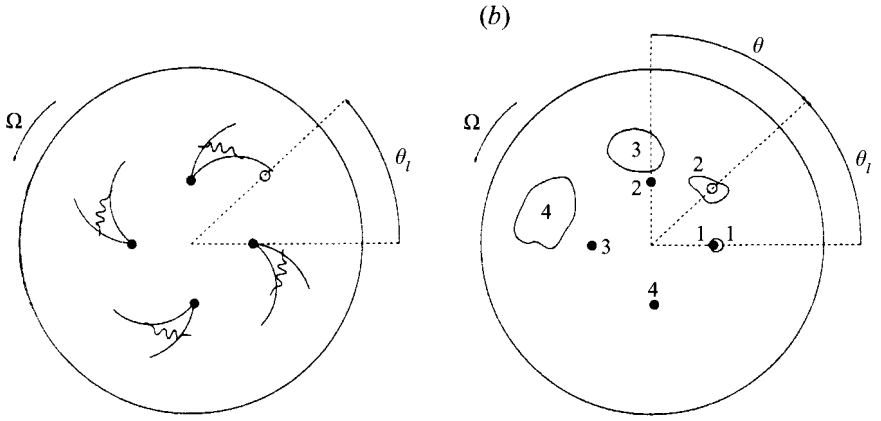

FIGURE 3. (*a*) A sketch of stationary disturbances generated by a fixed roughness (marked by a black circle) at equispaced instants in time: $t = 0,\ T/4,\ T/2,\ 3T/4,\ T,\ldots$. (*b*) A sketch of the evolution of a wave packet at four instants in time: $t = 0,\ T/4,\ T/2,\ 3T/4$, i.e. four hole positions (marked by a black circle). The small unfilled circles in (*a*) and (*b*) represent the hot-wire probe.

shaft is mounted vertically on a shaft driven by a d.c. servo-motor; both the shaft and the motor are an integral part of an air-bearing spindle. The design of the drive mechanism was chosen to minimize mechanical vibration of the system. The maximum out-of-flatness of the disk while it is rotating, which is predominantly due to a small imbalance of the disk rather than any surface roughness, is less than 1×10^{-6} m. The disk has constant angular velocity Ω to within 0.1%. A two-axis traverse mechanism, which carries a hot-wire probe, is mounted on a bar about 160 boundary-layer thicknesses above the disk. A smoothing screen, with a slit for the hot-wire probe to pass through, is positioned below the traverse mechanism to reduce the free-stream-turbulence level in the incoming axial flow. The horizontal axis of the traverse mechanism is operated by a linear motor and has a step resolution of 0.2 mm; the vertical axis is operated by a stepper motor with a step resolution of 0.0025 mm. These two axes allow the hot-wire probe to be moved to any radial position on the disk and to any useful height.

The disturbance of the flow over the top surface of the disk is introduced via a 0.2 mm diameter hole through the disk at a radius of 100 mm, i.e. the hole occupies just over 0.03% of the circumference. The nozzle producing the air jet has a diameter of 2 mm at exit and was positioned 2 mm below the entrance to the hole, on the underside of the disk. A pulse disturbance is created each time the hole passes over the nozzle, i.e. once per revolution of the disk. The amplitude of the pulse could be altered using a needle-valve pressure regulator.

Measurements taken by a hot wire that is free to move in r and z (the axial coordinate) but is fixed at some angular position in the laboratory frame θ_l (as is the case here) can be used to characterize the whole disturbance field generated by artificial fixed roughness elements. This is because fixed roughnesses excite waves that are stationary with respect to the disk, so the hot-wire probe, at constant r, will detect the same pattern of disturbance, apart from a shift in phase (depending on where the probe is relative to the roughness when sampling is triggered), for all θ_l. Figure 3 (*a*) shows a sketch of the disturbance pattern generated by a fixed roughness element at equispaced instants in time. The disturbance pattern, which is indicated by a trailing wedge, moves round with the roughness such that the hot-wire probe

measures the same disturbance at some point in the time series, as the wedge passes by, irrespective of its angular position θ_l. However, when the boundary layer is excited by an impulsive point source, hot-wire measurements are dependent on the position of the probe. This is illustrated by figure 3(*b*). The disturbance created by the initial pulse is pictured at four instants in time. The boundary layer is perturbed at position 1, which creates the wave packet also labelled 1. When the hole has reached $\theta_l = 90°$ ($t = T/4$), labelled 2, the wave packet has reached the position also labelled 2, and so on for positions 3 and 4. The hot-wire probe is pictured at $\theta_l = 45°$, where it measures part of the wave packet at $t = T/4$, at which time the packet lies at $\theta = -45°$ relative to hole, i.e. in the rotating reference frame. But at other values of θ_l (at the same radius) the probe would miss the wave packet completely. Thus, to track the developing wave packet and to resolve its structure, it is necessary to take measurements at closely spaced radial intervals and angular intervals. To change the relative angular position between the probe and the hole at the instant that the disturbance is generated, it is necessary to move the nozzle that supplies the jet of air. The nozzle can be moved around a circular ring, centred on the axis of rotation of the disk and attached below the disk, and clamped in the required position.

A single hot wire, of about 1 mm length and with a length-to-diameter ratio of about 250, was used to measure velocity perturbations. It was positioned parallel to the surface of the disk and aligned in the radial (circumferential) direction to measure circumferential (radial) velocities. The hot wire must be calibrated using a known flow velocity and in many experiments the free-stream velocity provides a convenient reference. However, for the rotating-disk flow there is no free-stream flow outside the boundary layer (apart from a small axial component); the only known speed is the rotational speed of the disk and therefore the speed of the flow at the surface of the disk. Clearly, the hot-wire probe cannot measure the flow speed at the surface of the disk. An alternative calibration method would be to use a separate calibration wind tunnel, but this would involve frequent removal of the hot-wire probe from its carrier. Each time the probe is removed and replaced, it needs careful re-alignment with the radial (circumferential) direction and the height of the wire from the disk must be remeasured. Furthermore, repeated removal of the probe increases the risk of damaging the wire. For these reasons, it was decided to calibrate the hot-wire by assuming that the mean velocity profiles are those given by boundary-layer similarity theory. By knowing the height of the wire from the surface and the speed of rotation, the mean velocity at the hot-wire position can be calculated. The hot wire can then be calibrated by measuring the mean output voltage from the hot-wire anemometer (averaged over 16384 sample points) for a range of mean flow speeds. While the anemometer was being calibrated, no input disturbance was applied to the boundary layer, therefore the only disturbances were those that occurred naturally. The mean flow speed measured by the probe can be varied by changing the rotational speed or by changing the radial position of the probe. Whenever possible, the rotation rate and position of the probe were chosen to correspond to a Reynolds number below the critical value for the onset of growing stationary disturbances. The assumption that the mean velocity profiles conform to those predicted by theory was checked and the results are discussed in §3.1. Any effects of the axial and radial (circumferential) mean velocity components on the calibration for the circumferential (radial) component were neglected. The hot wire was calibrated using a modified King's law to extend the low velocity range, which was taken from Johansson & Alfredsson (1982) and used more recently by Klingmann *et al.* (1993).

In order to calibrate the hot wire and to take measurements at specific heights

through the boundary layer, it is necessary to have a datum at a known distance from the surface of the disk. Each time the hot-wire probe was removed and replaced, an optical telescope was used to measure the distance between the hot wire and its reflection in the surface of the disk at a radial position close to the centre and a position close to the edge of the disk. Two radial positions were used to account for any non-parallelism between the disk and the horizontal traverse axis. Assuming a linear relation between distance from the disk and radius, a height datum was set for the included radial positions, to which all movements were referred so that the absolute distance from the disk could be calculated. In §3.1, it will be shown that measured mean velocity profiles match the theoretical profiles without any shift in height, which implies that this method of determining the height of the hot wire above the disk is satisfactory.

A computer, fitted with an analogue-to-digital (A–D) and digital-to-analogue converter was used to control the acquisition of data and the traverse. The sampling rate was chosen to be a constant multiple of the rotation rate, namely $S_r = 720\Omega$ Hz, where Ω is the speed of rotation of the disk in Hertz. This means that a constant number of data points were recorded per revolution of the disk, irrespective of the speed of rotation, i.e. 720 data points per revolution. Data logging was synchronized with the rotation of the disk by sampling the output signal from an optical tachometer on one of the A–D channels and triggering the start of data sampling when the rising ramp of the voltage pulse from the tachometer reached a threshold value. The voltage pulse from the tachometer could be made to coincide with the input of the flow disturbance. Before the signals generated by the hot-wire anemometer were logged, the signals were amplified and band-pass filtered to prevent aliasing, the high-pass and low-pass limits being 4 Hz and $S_r/2.5$, respectively. Ensemble averaging has been used to improve the signal-to-noise ratios of the measured time series; each ensemble-averaged time series contains 112 single realizations.

Further details on the experimental apparatus and procedure may be found in Lingwood (1995*b*, chap. 6).

3. Results and discussion

Unless otherwise stated, all measurements are plotted non-dimensionally, where the non-dimensionalizing length, velocity and time scales are $(\nu/\Omega)^{1/2}$, $r\Omega$ and $(\nu/\Omega)^{1/2}/(r\Omega)$, respectively, such that the non-dimensional radius is equivalent to R and the non-dimensional radial and circumferential mean velocities are equivalent to the von Kármán (1921) similarity variables.

3.1. *Mean velocity profiles*

Circumferential and radial mean velocity profiles were measured and are shown in figures 4(*a*) and 4(*b*), respectively, compared to the similarity profiles calculated by von Kármán (1921), which are only functions of the non-dimensional axial coordinate z. The velocity profiles were measured at radial locations and Ω corresponding to four different Reynolds numbers. The circumferential profiles $V_l(z)$ (where the subscript l indicates that the measurements are in the stationary laboratory frame) in figure 4(*a*) match the theoretical curve well, although the discrepancy does increase slightly at large z, where the mean velocities tend to zero. The agreement between the radial velocity profiles $U(z)$ (which is independent of whether measurements are taken in a stationary or rotating reference frame) and the theoretical curve shown in 4(*b*) is relatively good but, because the radial velocities are in general much smaller than the

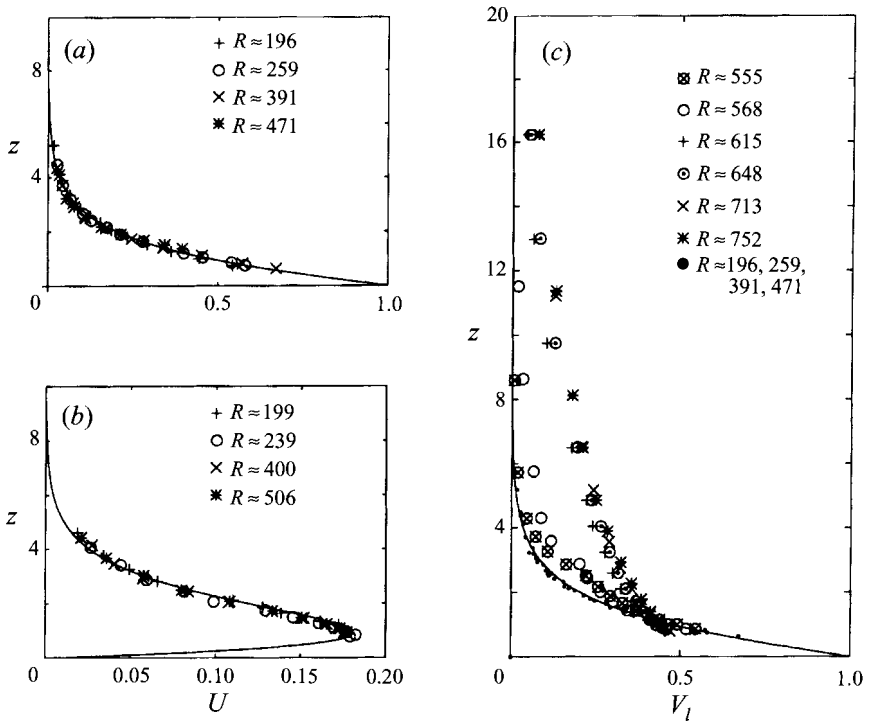

FIGURE 4. Mean velocity profiles at various Reynolds numbers: (*a*) circumferential velocities $V_l(z)$ (in the laboratory reference frame), (*b*) radial velocities $U(z)$, (*c*) circumferential velocities $V_l(z)$ into the turbulent regime. The solid lines indicate the theoretical profiles.

circumferential velocities, the radial velocities have lower signal-to-noise ratios. For this reason, the experimental measurements described later are circumferential, rather than radial, components of velocity. No axial components have been measured. There is good data collapse over the range of R shown, indicating laminar flow.

Figure 4(*c*) shows circumferential velocity profiles at Reynolds numbers corresponding to turbulent flows. The solid line and the dots are the same data as plotted in figure 4(*a*) and are included for reference. The profiles at $R \approx 555$ and $R \approx 568$ are significantly different from the theoretical laminar profiles, but they are not yet fully turbulent like those from $R \approx 615$ to $R \approx 752$, which are characterized by a much thicker boundary layer. Thus, as found in previous studies, it can be concluded that the boundary layer is transitional at $R \approx 555$ and $R \approx 568$, and fully turbulent by $R \approx 615$. The turbulent profile for $R \approx 752$ was measured within 5 mm of the edge of the disk, and yet it is similar to the other turbulent profiles. It seems that edge effects (i.e. deviations from the theoretical behaviour, which assumes an infinite disk) are minimal.

Note that no shift has been applied to the data points plotted in figure 4. This indicates that the positioning of the hot-wire probe at a particular height in the boundary layer, described in §2, is sufficiently accurate for these purposes.

3.2. *The unexcited flow*

3.2.1. *Time series for the unexcited flow*

During this investigation the hole was taped over on the underside of the disk, but the exit hole on the topside was not plugged in any way. Measurements were taken at $z = 1.3$, because the velocity perturbations have a maximum at about this height (see §3.2.3).

The process of ensemble averaging a number of individual time series has the effect of reducing the amplitude of features that are not repeated in those time series. Thus, if an artificial roughness element, which excites modes that are stationary with respect to the disk, were put on the disk then the repeatable features would be stationary and the effects of naturally occurring random excitation from free-stream turbulence would not be seen in the ensemble-averaged record. Here, there are no artificial roughness elements, as such, but there are likely to be small dust motes and surface imperfections that excite repeatable disturbances from one revolution to the next. Accordingly, the ensemble-averaged time series shown in this section highlight stationary disturbances and give no information on random travelling disturbances in the boundary layer. It follows that ensemble averages disguise the onset of transition, because localized turbulent bursts occur randomly through the individual time series and, while repeatable structures remain, the ensemble-averaged record can look similar to those from a laminar flow. However, the standard deviations of the individual realizations away from the ensemble average, and individual realizations themselves can be used to assess the true nature of the flow.

The behaviour of the boundary layer might be expected to be the same, provided the Reynolds number is the same, irrespective of physical position and speed of rotation. But it is conceivable that the speed of rotation has an effect on receptivity mechanisms, enhancing or inhibiting the process of internalizing disturbances. If this were the case, then the speed of rotation would influence the extent to which the hole acts as a source of stationary modes, as well as the extent to which other unavoidable sources excite the boundary layer. This conjecture has not been studied in detail, but sets of measurements were taken at two disk speeds: $\Omega = 1000$ and 1400 r.p.m. Figures 5(*a*) and 5(*b*) show peak-normalized (a form in which it is easier to see the origins of the stationary disturbances) time series of the circumferential perturbation velocity v at $\Omega = 1000$ r.p.m. and $\Omega = 1400$ r.p.m., respectively. The vertical placement of each time series is proportional to its non-dimensional radial position, i.e. proportional to its Reynolds number, and each trace covers one revolution of the disk. The measurements in figures 5(*a*) and 5(*b*) are plotted to the same scale and, apart from the lowest two traces, they were taken at the same physical radii but, because Ω is larger in figure 5(*b*), the corresponding Reynolds numbers are larger and the time series extend further into the turbulent regime. The traces labelled $R \approx 266$ and $R \approx 311$ in figures 5(*a*) and 5(*b*), respectively, correspond to the radial positions at which the hole lies.

In both figures 5(*a*) and 5(*b*), if the hole were generating stationary disturbances, there would be a wedge of instability waves originating from the third trace from the bottom at $t = 0$. At $\Omega = 1000$ r.p.m. there does not seem to be any such disturbance pattern. However, at $\Omega = 1400$ r.p.m. there is a wedge of disturbances that seems to originate in the region of the hole. This difference could simply be due to the higher Reynolds number at the hole for figure 5(*b*), or it could be that the increased disk speed enhances the receptivity of the boundary layer to stationary disturbances. In both cases, there is a source of stationary disturbances that lies at a radius of

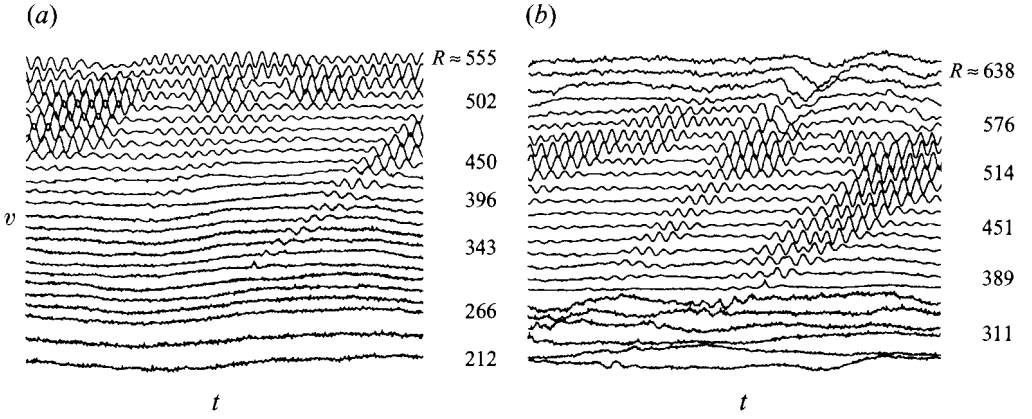

FIGURE 5. Peak-normalized ensemble-averaged time series of v, lasting one time period and measured at $\theta_i = 0°$, various radial locations and $z = 1.3$: (*a*) $\Omega = 1000$ r.p.m., (*b*) $\Omega = 1400$ r.p.m.

about 120 mm (seventh trace from the bottom) and $t/T \approx 0.57$, which corresponds to $\theta \approx -205°$ (205° from the hole in the opposite direction to the rotation). The disturbances originating from the second source are larger than those created by the hole, suggesting that the hole is less of a source of stationary disturbances than unavoidable sources, such as dust and surface imperfections.

For Reynolds numbers of about 622 and above, there are no repeatable structures remaining and the behaviour is fully turbulent. This is consistent with measurements of the mean circumferential velocity profiles, given in figure 4(*c*), where the profile is characteristic of a fully turbulent boundary layer for Reynolds numbers above about 615. For both figures 5(*a*) and 5(*b*), the peak amplitude of v is about 0.03 at $R \approx 500$ (i.e. 3% of the local disk speed) and only about 7×10^{-4} at the Reynolds number corresponding to the hole. As mentioned in the introduction, Balachandar *et al.* (1990) performed an analysis of the rotating-disk boundary layer that showed that at $R = 500$ a primary disturbance root-mean-square amplitude of about 9% is needed for the onset of secondary instabilities. The results of this study imply that here the stationary disturbances are sufficiently small, even close to the onset of transition, for the boundary-layer stability to be governed by the mean velocity profiles rather than secondary instabilities.

Figure 6 shows typical single realizations included in three of the ensemble-averaged time series in figure 5(*b*) at Reynolds numbers in the region corresponding to the onset of transition. Figure 6 also shows the standard deviations σ associated with these data sets, plotted as non-dimensional velocities and to the same scale as the single realizations for ease of comparison. At $R \approx 497$, σ is so small compared with its peak values at $R \approx 514$ and $R \approx 530$ that it is hardly visible in figure 6(*b*). At $R \approx 514$, in figures 6(*c*) and 6(*d*), σ is generally larger and has two pronounced peaks between $t/T = 0.8$ and $t/T = 0.9$, which indicate that the features in the time series at these times were unrepeatable from realization to realization. The peak value of σ at $R \approx 514$ is nearly six times larger than the peak value at $R \approx 497$. This sudden increase in σ from a nearly constant low level at Reynolds numbers below $R \approx 514$ suggests that there is a sudden increase in the amplitudes of random events at about this Reynolds number and that transition from laminar to turbulent flow begins between $R \approx 497$ and $R \approx 514$. The same behaviour is observed at these Reynolds numbers when $\Omega = 1000$ r.p.m. Figures 6(*e*) and 6(*f*) show that by Reynolds

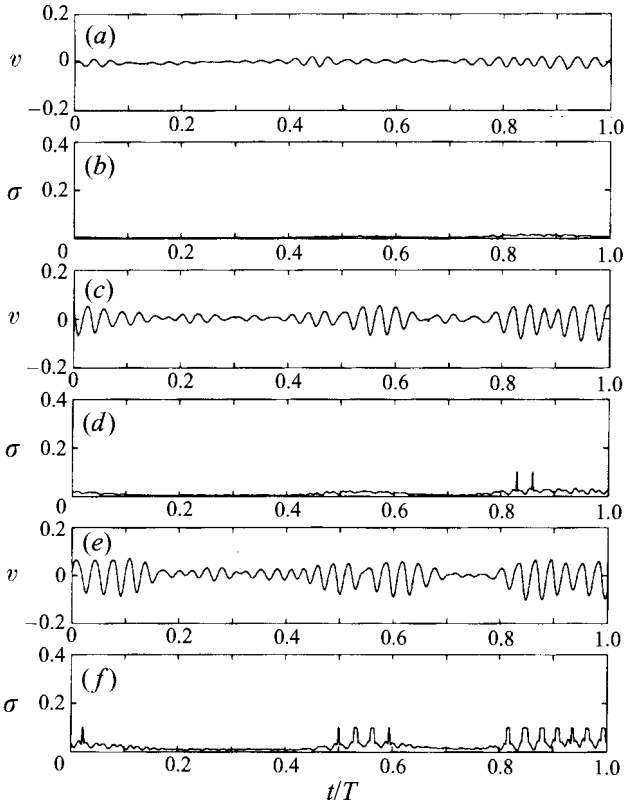

FIGURE 6. Examples of single realizations included in three of the ensemble-averaged time series, given in figure 5(*b*), and σ associated with these ensemble averages: (*a,b*) $R \approx 497$, (*c,d*) $R \approx 514$, (*e,f*) $R \approx 530$.

numbers of about 530, a large part of the time series is highly unrepeatable and the boundary-layer behaviour is increasingly nonlinear. The time series, however, is still characterized by interacting packets of waves, originating from separate sources, and does not look significantly different from the laminar time series. Chin & Litt (1972) also mentioned the persistence of stationary vortices in the transitional flow, and they suggested that the vortices remain attached to the surface in the viscous sublayer. The dominant features of σ in figure 6(*f*) are regions of periodicity between $t/T = 0.5$ and $t/T = 0.6$ and between $t/T = 0.8$ and $t/T = 1.0$, in which the peaks of σ are, in general, aligned with troughs in the time series, which indicates that from one realization to the next the amplitude of the these troughs is highly variable relative to the neighbouring peaks in the time series. The same features were observed by Shaikh (1993) in the Blasius boundary layer, where peaks in σ in the transitional region of the flow were found to be associated with troughs in the time series and the largest of these peaks developed downstream into turbulent spots. Poll (1985), for the flow round a yawed cylinder, and Healey (1995), for the Blasius flow, also noted that sufficient modulation of the mean velocity profiles causes the profiles to become inflectional and highly unstable to travelling waves. The alignment of peaks in σ with troughs in v could be related to this instability. In a few cases, for example at $t/T \approx 0.59$ in figure 6(*f*), the peak in σ is aligned with a maximum in the gradient of v, which could be due to varying phase of the wave from one realization to the next.

Figure 7 shows typical single realizations included in four of the ensemble-averaged

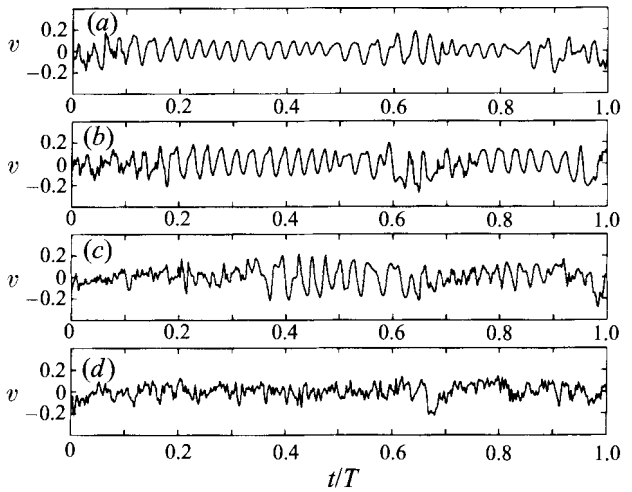

FIGURE 7. Examples of single realizations included in four of the ensemble-averaged time series, given in figure 5(*b*): (*a*) $R \approx 559$, (*b*) $R \approx 575$, (*c*) $R \approx 591$, (*d*) $R \approx 606$.

time series given in figure 5(*b*) at high Reynolds numbers. At $R \approx 559$, in figure 7(*a*), there is a region of high-frequency oscillation at the beginning of the time series. This region expands with increasing Reynolds number and at $R \approx 606$, in figure 7(*d*), the time series appears fully turbulent, although the corresponding ensemble-averaged time series in figure 5(*b*) still has remnants of the periodicity associated with the stationary waves.

In passing, it is worth noting a common feature of the time series measured at Reynolds numbers above about 450 and before fully turbulent behaviour sets in, namely kinks in the time series at points where two wave packets, which have originated from different sources, merge. For example, figure 8 shows an ensemble-averaged time series measured at $R \approx 502$, where two such kinks are shown at $t/T \approx 0.37$ and $t/T \approx 0.87$. As suggested by Le Gal (1992), these kinks seem to arise because of a phase difference between two merging wave packets. Kinks in time series have also been associated with secondary instabilities (Kohama 1987; Wilkinson & Malik 1985), but these were observed within a wave packet and not where individual packets merge. For example, figure 11 of Wilkinson & Malik (1985), which is for a study of natural transition of the rotating-disk boundary layer, shows a time series with a kinked central region that is explained as inflections of the primary vortices, i.e. secondary instabilities. This behaviour was found to be most prominent in a range of transitional Reynolds numbers that shifted to lower Reynolds numbers (between $R \approx 520$ and $R \approx 530$) when an artificial roughness (0.13 mm high by 0.64 mm square) was placed on the disk at $R = 249$. No such behaviour was observed here before the onset of turbulent bursts although, perhaps, there are occasional kinks in figure 7(*b*) at $R \approx 575$ between $t/T = 0.2$ and $t/T = 0.5$, but nothing with the degree of periodicity observed by Wilkinson & Malik (1985). Thus, it is suggested that, in this case, secondary instabilities do not play an important part in the onset of transition from laminar to turbulent flow, although they might if the surface roughness were larger causing primary stationary vortices with larger amplitudes.

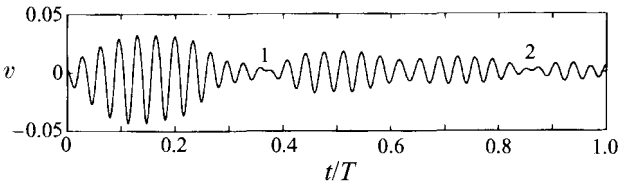

FIGURE 8. A closer view of the $R \approx 502$ ensemble-averaged time series given in figure 5(*a*), showing two kinks: one at $t/T \approx 0.37$ (labelled 1), the other at $t/T \approx 0.87$ (labelled 2).

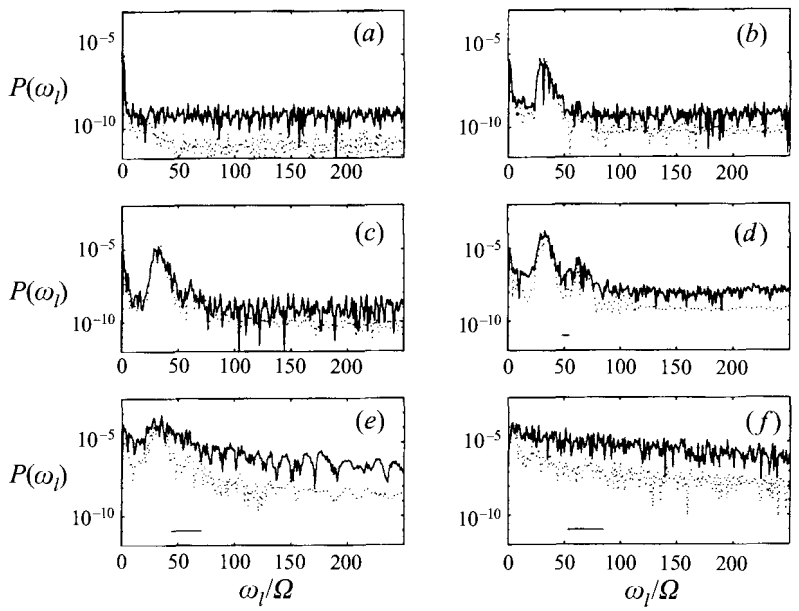

FIGURE 9. Fourier power spectra for single-realization time series (——) and ensemble-averaged time series (· · · · · ·) for $\Omega = 1400$ r.p.m. and $z = 1.3$ for the unexcited boundary layer: (*a*) $R \approx 281$, (*b*) $R \approx 482$, (*c*) $R \approx 497$, (*d*) $R \approx 514$, (*e*) $R \approx 560$, (*f*) $R \approx 622$. For $R > 510$, the horizontal solid lines indicate the absolutely unstable frequencies.

3.2.2. *Power spectra for the unexcited flow*

Fourier power spectra were calculated to show the frequency content of the time series discussed above. For example, figure 9 shows power spectra for six different Reynolds numbers, calculated from single-realization time series and ensemble-averaged time series both measured at $\Omega = 1400$ r.p.m. and $z = 1.3$. The spectral amplitudes $P(\omega_l)$ are plotted against the non-dimensional quantity ω_l/Ω, where ω_l is the angular frequency of oscillation measured by the hot-wire anemometer in the laboratory reference frame. Note that $\omega_l/\Omega = \omega/\Omega + \beta$, where ω is the disturbance frequency in the rotating frame and β is the circumferential wavenumber, therefore stationary vortices (for which $\omega = 0$ by definition) are characterized by values of $\omega_l/\Omega = \beta$ and oscillations associated with the small imbalance of the disk rotation have $\omega_l/\Omega = 1$. Normally, neutral-stability curves are given for stationary waves, where branch 1 has higher ω_l than branch 2, but for travelling waves the situation is more complicated. The power spectra were calculated from periodic (non-dimensional) circumferential velocity time series as one-sided spectra, i.e. extending from $\omega_l = 0$ to $\omega_l = S_r/2.5$ (the sampling frequency).

The broad-band content of turbulent spectra is expected to be more pronounced

in spectra of single-realization time series than those of ensemble-averaged data. Single-realization time series include non-deterministic non-stationary waves ($\omega \neq 0$), because these components are not averaged away by the ensembling process. Accordingly, single-realization power spectra may show features not included in the ensemble-averaged spectra, which necessarily show only repeatable disturbances, such as those generated by fixed roughnesses. The dominant feature of the power spectra for $R \approx 278$, in figure 9(*a*), is a spike in $P(\omega_l)$ at $\omega_l/\Omega = 1$, which is due to the imbalance of the disk and this part of the curve can be disregarded. Other frequencies have a uniformly low background-noise spectrum. As expected, the ensemble-averaged spectrum has a lower background-noise level. At $R \approx 482$, in figure 9(*b*), there is a band of ω_l in both the single-realization and ensemble-averaged spectra where $P(\omega_l)$ is large, with a maximum amplitude at $\omega_l/\Omega \approx 30$, superimposed on a very similar background spectrum to that in figure 9(*a*). The agreement between the single-realization and ensemble-averaged peak in $P(\omega_l)$ suggests that this peak describes predominantly stationary disturbances. At $R = 482$, linear theory predicts that stationary modes are unstable for values of β (and therefore ω_l/Ω) between about 20 and 60, a range that approximately describes the large-amplitude frequencies in figure 9(*b*). In the experiment, the largest components are those that have been convectively unstable below this Reynolds number and have therefore had more space in which to grow. The shape of the neutral-stability curve for stationary modes implies that frequencies with the largest amplitudes are likely to be closer to the lower end of the unstable range, i.e. closer to $\omega_l/\Omega = 20$, because these are the frequencies that become unstable first. As expected, the 28–32 stationary vortices observed in visualization experiments are not the product of a single wavenumber, but are due to a superposition of wavenumbers (Mack 1985; Wilkinson & Malik 1985). At $R \approx 497$, in figure 9(*c*), both power spectra are qualitatively similar to those at $R \approx 482$. The peak is larger than at $R \approx 482$, but occurs at about the same frequencies and the background-noise levels at the two Reynolds numbers are quantitatively similar. Again, the agreement between the single-realization and ensemble-averaged fundamental peaks and the small harmonic peaks, centred on $\omega_l/\Omega \approx 60$, suggests that these features are well described by the ensemble-averaged signals and are stationary with respect to the disk. The appearance of a harmonic component shows that there is some nonlinear behaviour but, because there is little broadening of the spectra, this nonlinearity does not seem sufficient to cause the onset of transition. However, at a slightly higher Reynolds number there is a sudden change in the nature of the spectra. At $R \approx 514$, shown in figure 9(*d*), there is about a tenfold increase in the background-noise level (in both the single-realization and ensemble-averaged spectra) as well as a tenfold increase in the fundamental and the harmonic peak. Figures 9(*e*) and 9(*f*) show power spectra for $R \approx 560$ and $R \approx 622$, respectively, where there is a general broadening and increase in amplitude of the spectra. At $R \approx 622$, there is no longer any sign of the peak associated with the primary stationary vortices and the flow is fully turbulent.

Power spectra were also calculated from time series measured with the disk rotating at 1000 r.p.m. The spectra are similar to those in figure 9. Between $R \approx 502$ and $R \approx 514$, there is a general broadening of the spectra and the background-noise levels of both the single-realization and ensemble-averaged spectra increase about tenfold from a constant low level.

Absolutely unstable frequencies, calculated by Lingwood (1995*a*), are indicated in figures 9(*d–f*) by a horizontal solid line. Because calculation of the absolute frequencies was based on a local stability analysis, which assumes a locally parallel

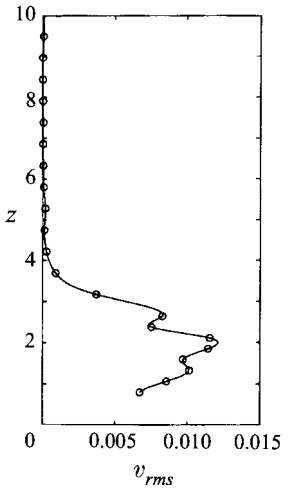

FIGURE 10. Profile of v_{rms} for the unexcited boundary layer at $R \approx 502$ and $\Omega = 1000$ r.p.m., calculated from ensemble-averaged data.

flow, it is not clear at what exact frequency absolute growth of disturbances would be expected in the true spatially varying boundary layer. Nonetheless, as discussed by Koch (1985), linear theory gives a useful first approximation of the global frequencies, but nonlinear theory, which is outside the scope of the present work, is needed for comparison of theoretical and experimental disturbance amplitudes. It is unfortunate that for measurements made in the laboratory reference frame, the absolutely unstable frequencies intersect with the harmonic frequencies of the primary stationary vortices (in a rotating frame the absolute frequencies are negative but, combined with positive β, ω_l is positive), making it difficult to assess whether there is growth in the spectral components associated with the absolute frequencies. Furthermore, it is travelling modes that become absolutely unstable and these are randomly excited and therefore can only be expected in the single-realization power spectra. However, the single-realization power spectra do not show a well-defined absolute frequency ensuing close to the critical Reynolds number for the onset of absolute instability, but results from the excited flow, given in the next section, provide more direct evidence that the flow becomes absolutely unstable.

3.2.3. *The axial structure of the unexcited disturbance field*

To characterize the z-structure of the unexcited disturbance field, the root-mean-square (denoted by the subscript *rms*) amplitudes of circumferential velocity perturbations were calculated. For example, figure 10 shows a profile of v_{rms} at $R \approx 502$. The data points (o) have been interpolated with cubic-spline fits to produce an approximate curve of the perturbation profile. As expected, the perturbations decay at large z and, although there are not enough points to be sure, figure 10 appears to have three maxima: at $z \approx 1.3$, $z \approx 1.9$ and $z \approx 2.7$. The maximum at $z \approx 1.9$ is the largest at this Reynolds number. Nevertheless, for general circumferential measurements, where only one height in the boundary layer was considered, $z = 1.3$ was the chosen position because the disturbances are close to their maximum at this position and because the mean circumferential velocity is greater there than at the higher maxima, giving a more accurate hot-wire calibration.

To further illustrate the effect that perturbations have on the mean flow, figure 11 shows instantaneous circumferential velocities at four Reynolds numbers ($\Omega =$

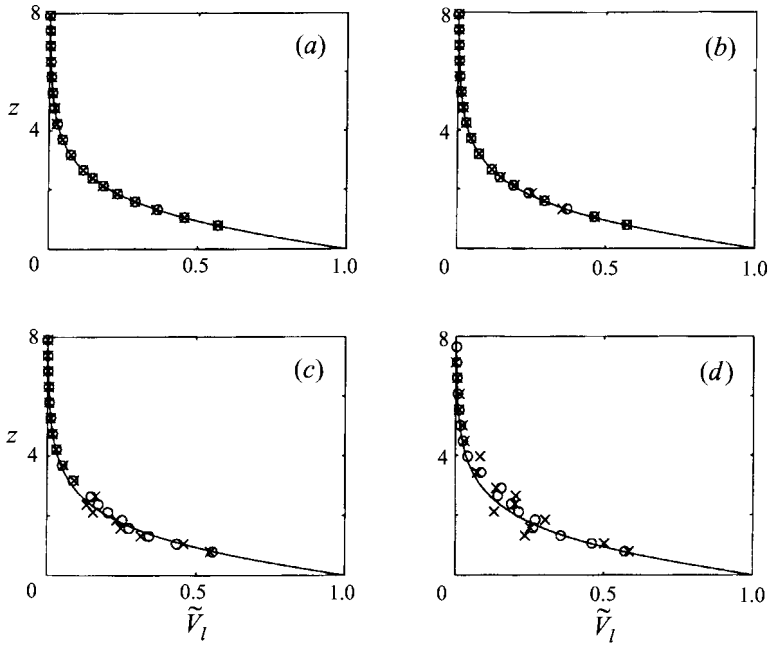

FIGURE 11. Instantaneous circumferential velocities for the unexcited boundary layer: (*a*) $R \approx 450$, $t/T \approx 0.93$; (*b*) $R \approx 476$, $t/T \approx 0.58$; (*c*) $R \approx 502$, $t/T \approx 0.18$; (*d*) $R \approx 528$, $t/T \approx 0.19$. Solid lines give the theoretical mean circumferential profile, ○ mark instantaneous profiles taken from ensemble-averaged time series and × mark the scatter from single-realization time series.

1000 r.p.m. and $\theta_l = 0°$). The solid line gives the theoretical mean circumferential profile, the circles mark instantaneous profiles of $\tilde{V}_l = V_l + v$, calculated from ensemble-averaged perturbation data and using the theoretical mean velocity V_l, and the crosses indicate the scatter due to randomly excited travelling waves taken from single-realization time series. The time instant for each plot is chosen to include the maximum single-realization value of v at the respective Reynolds numbers. Thus, the instantaneous velocities show the maximum mean-flow distortions that occur in one revolution of the disk.

Clearly, for $R \approx 450$ and $R \approx 476$ the instantaneous velocities lie close to the theoretical mean profile; the maximum disturbance amplitudes (derived from the ensemble-averaged data) are about 0.23% and 1.8%, respectively. By $R \approx 502$ the maximum disturbance amplitude has increased to about 3.4% and 6.1% for ensemble-averaged and single-realization data, respectively, and there is a more noticeable distortion of the mean-flow profile in figure 11 (*c*). But, on either basis, these maximum amplitudes are still less than the threshold amplitude (9%) predicted by Balachandar *et al.* (1990) for the onset of secondary instabilities at $R = 500$. Furthermore, the results given in §3.2.1 do not indicate the presence of secondary instabilities before the onset of transition. Thus, it is likely that use of the theoretical mean profile in linear-stability analyses is still justifiable at this Reynolds number. However, by $R \approx 528$ the mean-flow distortion shown in figure 11 (*d*) is significant and the power spectra, shown in figure 9, indicate that the flow has become transitional. The instantaneous profile based on ensemble-averaged data has a maximum amplitude of about 7.3%, which could perhaps be considered small enough for the theoretical mean profile to be used in a linear-stability analysis, but the instantaneous velocity

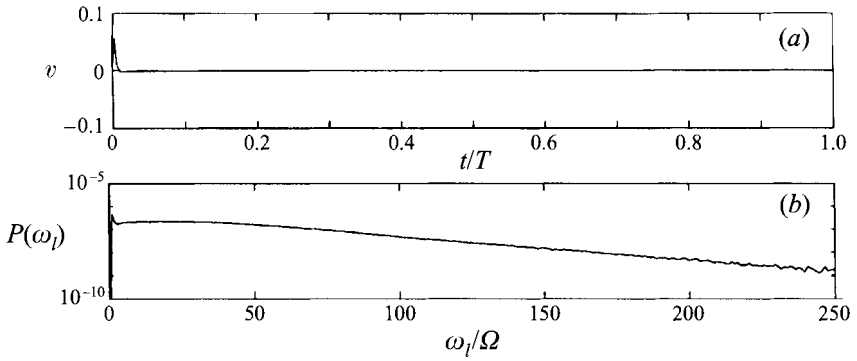

FIGURE 12. (*a*) Ensemble-averaged time series at $R \approx 266$, $\theta_l = 0°$ and $z = 1.3$. (*b*) Power spectrum calculated from the time series shown in (*a*).

that includes random travelling disturbances and possibly high-frequency oscillations associated with turbulent bursts now has a maximum amplitude of over 14%.

Note that the mean velocity profiles in figure 4 are derived from average velocities over many revolutions of the disk at particular heights in the boundary layer and therefore result from the average of instantaneous profiles, such as those in figure 11, at many successive times.

3.3. *The excited flow*

The boundary layer was excited impulsively once per revolution of the disk through a 0.2 mm hole at a radius of 100 mm. The amplitude of the pulsed disturbance was sufficiently large for the wave-packet development to be tracked easily, without being large enough to bypass the linear stages of development, or to be unrepeatable from one realization to the next. If the amplitude of the input disturbance was too large, localized turbulent spots were generated, which then propagated through the otherwise laminar boundary layer. It has yet to be determined whether this affects the position of the transition front. Figure 12(*a*) shows the pulse, with the hot-wire probe positioned directly over the hole ($z = 1.3$) at the time of excitation ($t/T = 0$), with $\Omega = 1000$ r.p.m. The disturbance generated by the pulse is sharp and impulse-like, as required to excite a broad spectrum of frequencies, and there is very little overshoot, i.e. negative disturbances around the main pulse, as was the case with the acoustic forcing of the rotating-disk boundary layer performed by Wilkinson *et al.* (1989). Figure 12(*b*) shows the power spectrum $P(\omega_l)$ calculated from the time series shown in figure 12(*a*). Clearly, the pulsed disturbance excites a broad range of frequencies. The spectrum is particularly flat for frequencies up to fifty times the disk frequency, beyond which there is a steady decrease in the amplitude of $P(\omega_l)$ due to the small, but finite, width of the pulse.

3.3.1. *Time series for the excited flow*

As discussed in §2 with the aid of figure 3(*b*), it is necessary to take measurements at angular and radial intervals to characterize the development of the wave packet generated by the point source. Accordingly, measurements were taken at 10° intervals, covering 360°, and at 5 mm radial intervals, between 90 mm and 210 mm. Measurements were taken at these positions with the disk spinning at 1000 r.p.m. and 1400 r.p.m., so that the radial ranges correspond to Reynolds numbers of 238–555 and 280–654, respectively, and giving Reynolds numbers of about 266 and 311, re-

spectively, at the source position. In this section, all measurements were taken at $z = 1.3$.

Figure 13 shows a small selection of ensemble-averaged time series, each lasting one time period, of the circumferential perturbation velocity v at different angular positions of the hot-wire probe. The vertical placement of the time series in each plot is proportional to its radius or Reynolds number. The externally applied pulse is clearly visible in figure 13 (*a*) at $t = 0$ and $R \approx 311$. The start of every time series coincides with the time at which the boundary layer is perturbed. The generated wave packet initially moves radially outwards and moves forwards in θ_l, but does not keep pace with the angular position of the hole and therefore falls increasingly behind, in much the same way as sketched in figure 3 (*b*), and the radial and angular extent of the packet increases with time. For instance, at $t/T = 0.5$, when the hole has moved through half a turn, the wave packet has moved through about 60° (see figure 13 *b*).

By the time the wave packet has reached $\theta_l = 80°$ the disk has completed one revolution since the initiation of the pulse, and figure 13 (*e*) shows the packet after a second revolution of the disk. In the second revolution, the trailing edge of the packet moves through $\theta_l \approx 140°$ compared with $\theta_l \approx 80°$ in the first revolution, which implies an increasing circumferential propagation velocity with increasing Reynolds number. The radial propagation velocity of the wave packet is better shown by later figures. The packet does not progress much beyond $R \approx 520$ before its smooth structure is destroyed by bursts of turbulence, characteristic of the onset of transition, in regions of large-amplitude fluctuations. By $R \approx 615$ the time series look fully turbulent.

Having followed the wave-packet development through to $\theta_l = 300°$, in figure 13 (*f*), further development can be traced through $\theta_l = 360° = 0°$ (figure 13 *a*), and so on, although by this stage the wave packet has almost completely merged with the radial band of transitional flow that exists at all angles.

As well as the dominant travelling waves excited by the localized pulse, there are also stationary waves excited by fixed roughnesses on the disk. In fact, the wave-packet disturbances are superimposed on an unexcited disturbance environment, as discussed in §3.2. Figure 14 shows an expanded view of a section of figure 13 (*a*). Here, each ensemble-averaged time series is peak normalized to show small disturbances that are not otherwise visible. In particular, figure 14 shows stationary disturbances generated by a surface imperfection at a radius of about 120 mm ($R \approx 373$ at $\Omega = 1400$ r.p.m.) and $\theta \approx -205°$ (see §3.2).

The development of the wave packet, which is in (r,θ_l,t)-space, can be projected onto (r,t)-space, to assess the radial propagation of the packet. Figure 15 (*a*) shows the progression of the wave packet for four disk revolutions, where $z = 1.3$ and $\Omega = 1400$ r.p.m. This figure consists of an overlay of thirteen contour plots, each corresponding to a different θ_l, ranging from 0° to 330°. For clarity, only one contour level has been plotted, namely the 0.008 amplitude level (0.8 % of the local disk speed) of the envelope function $e_v(t;\theta_l)$, which is illustrated in figure 16. The definition for the envelope function is taken from Gaster & Grant (1975), namely $e_v = (v_r^2 + v_i^2)^{1/2}$, where v_r is the velocity record and v_i is the original velocity record with the phase of all frequencies shifted through 90°, which is conveniently constructed in Fourier space and is equivalent to the Hilbert transform of v_r.

Figure 15 (*b*) shows the leading and trailing edges of the wave-packet trajectory derived from figure 15 (*a*). Lines have been fitted, in a least-squares sense, to the data points. Both lines were constrained to pass through the source position at $R \approx 311$ and $t = 0$. The leading edge is modelled by a straight line with gradient 0.0038, which corresponds to a velocity of about 1.97 m s^{-1}, while the trailing edge is modelled as

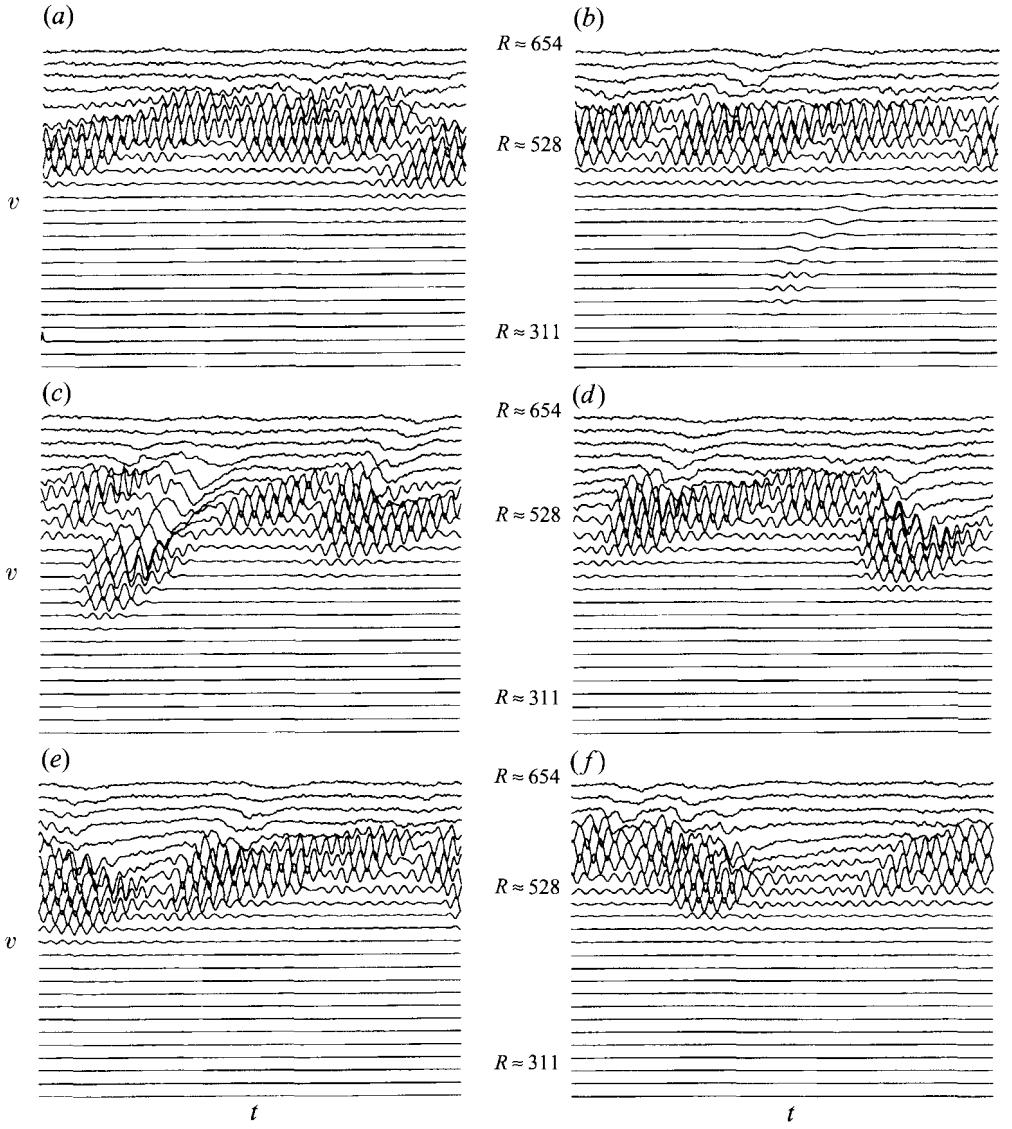

FIGURE 13. Ensemble-averaged time series of v for the excited boundary layer at $z = 1.3$ and $\Omega = 1400$ r.p.m: (*a*) $\theta_l = 0°$, (*b*) $\theta_l = 60°$, (*c*) $\theta_l = 140°$, (*d*) $\theta_l = 220°$, (*e*) $\theta_l = 260°$, (*f*) $\theta_l = 300°$

an asymptote to the critical Reynolds number for the onset of absolute instability, and is given by

$$t/T \approx 0.011r - 3.57 + 27.08/(510 - r). \tag{3.1}$$

This choice of model for the trailing edge was influenced by local linear-stability theory, in which the steepest-descent method can be used to calculate the time-asymptotic approximation to the impulse response in a quasi-parallel flow (e.g. Huerre & Monkewitz 1985, 1990) and the criterion for absolute instability of the flow is growth of disturbances along the 'ray' for which $(r - r_s)/t = 0$ (r_s is the source radius), i.e. temporal growth in a reference frame that has zero velocity in the radial direction, so in either the laboratory or the rotating reference frame (see figure 1*b*). Here, in a flow that is non-parallel in the sense that the Reynolds number varies with

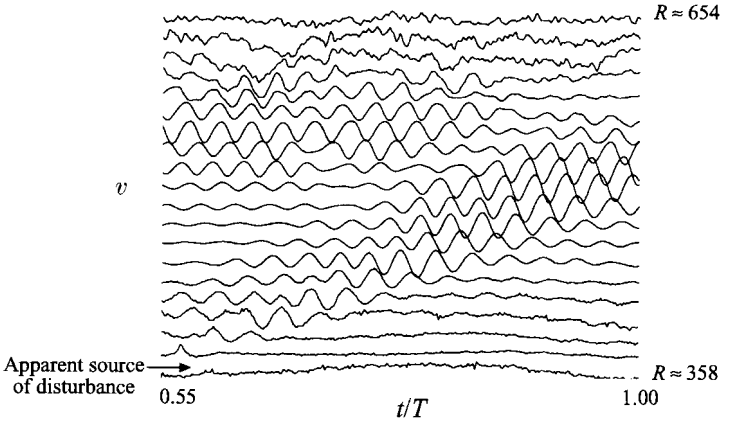

FIGURE 14. Expanded section of figure 13 (*a*) showing peak-normalized ensemble-averaged time series.

radius and that is thought to become absolutely unstable at a particular Reynolds number, it is expected that there will be temporal growth of disturbances along the ray $(r - r_c)/t = 0$, where r_c is the radius at which the non-parallel flow becomes absolutely unstable. Below this radius the flow is convectively unstable. In order to match the absolutely unstable behaviour to the preceding convectively unstable behaviour, it seems likely that the trailing edge, or ray, of the disturbance tends towards the vertical as it approaches the critical radius for the onset of absolute instability, i.e. approaches $(r - r_c)/t = 0$ as sketched in figure 1 (*c*). In figure 15 (*b*) the trailing edge was constrained to asymptote towards a critical radius of 510, which is the location for the onset of absolute instability derived from a local linear-stability analysis (Lingwood 1995*a*). Clearly, this value may not apply exactly to the true non-parallel flow, but the experimental points marking the trailing edge in figure 15 (*b*) do closely follow the predicted behaviour. The wave packet is undoubtedly convective at low Reynolds numbers, it is limited by rays with positive gradient as it convects outwards from the source, and spreads both radially and temporally with increasing Reynolds number. However, the radial wave-packet propagation is limited, such that the packet is no longer defined for Reynolds numbers much above 500, but continues to convect circumferentially even when its radial leading edge is disintegrating. The wedge of instability encompassing the wave packet tends towards the vertical in figures 15 (*a*) and 15 (*b*) as the critical Reynolds number for the onset of absolute instability is approached. This causes a build-up of energy at Reynolds numbers close to the calculated critical value for the onset of absolute instability and leads to a final state determined by nonlinear effects.

Note that the stationary disturbances do not show this type of behaviour. For instance, figure 17 shows a contour plot of the envelope function for stationary disturbances taken from figure 5 (*b*). Included in figure 17 are wedges of instability originating from two fixed roughnesses: the hole used for disturbing the flow and a second source of stationary disturbances (see §3.2) at a radius of about 120 mm ($R \approx 373$ at $\Omega = 1400$ r.p.m.) and $t/T \approx 0.57$, which corresponds to $\theta \approx -205°$. The trailing edge of the stationary disturbances reach a radius of 510 in $t \approx 3T/4$ from their initiation in marked contrast to the travelling waves. The bounding rays have approximately constant gradient with increasing Reynolds number, implying that the stationary disturbances remain convective up to transitional Reynolds numbers. Note that the

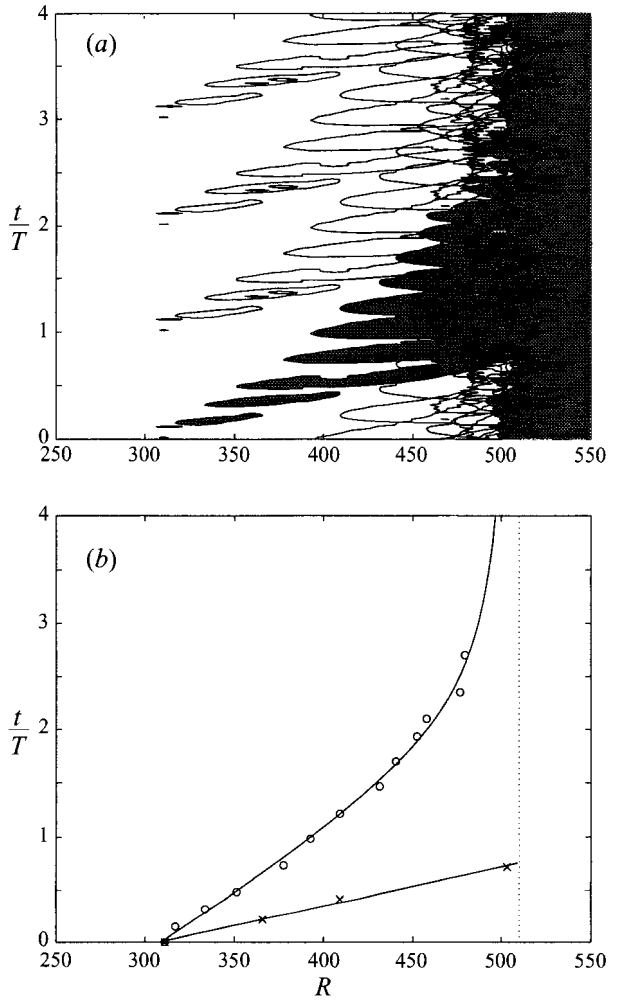

FIGURE 15. (*a*) Contour plot, at the 0.008 level, of the wave-packet envelope at $z = 1.3$, $\Omega = 1400$ r.p.m. and $\theta_l = 0°$, 20°, 40°, 60°, 90°, 120°, 150°, 180°, 210°, 240°, 270°, 300°, 330°. (*b*) Leading edge (×) and trailing edge (○) of the wave-packet trajectory, taken from (*a*), and least-squares fits to the experimental data (——). The critical Reynolds number for absolute instability, 510, is indicated by a dotted line.

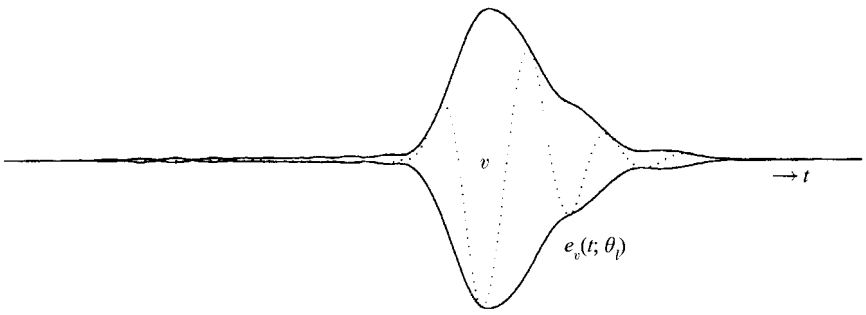

FIGURE 16. Time series (· · · · · ·) and the associated envelope function (——) for the excited boundary layer at $R \approx 425$, $z = 1.3$, $\theta_l = 90°$ and $\Omega = 1000$ r.p.m. The origin of the time series has been shifted so that the packet lies more centrally.

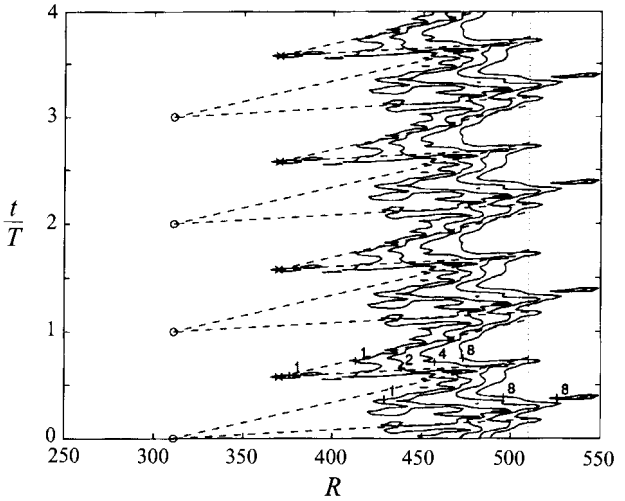

FIGURE 17. Contour plot of the envelope function for stationary disturbances, at levels 0.001, 0.002, 0.004 and 0.008 (marked by 1, 2, 4 and 8, respectively), at $z = 1.3$, $\Omega = 1400$ r.p.m. and $\theta_l = 0°$, for four revolutions of the disk. The leading and trailing edges have gradients of about 0.0090 and 0.0038, respectively. The hole in the disk and a second source of stationary disturbances are indicated by ○ and ×, respectively, and a dotted line marks $R = 510$.

trailing edge of the stationary disturbances has a gradient of about 0.0038, which is approximately the same as the leading edge of the travelling disturbances in figure 15.

3.3.2. *Power spectra for the excited flow*

As for the unexcited boundary layer, Fourier power spectra have been calculated to determine the frequency content of the time series discussed above. There are spectra available at every radial location and all θ_l-positions for the two disk speeds considered, but only a limited selection will be presented here. Figure 18 shows examples of power spectra calculated from ensemble-averaged time series, shown as contour plots of $\log(P(\omega_l))$ for $\Omega = 1400$ r.p.m. and a range of θ_l. The shading marks the high and low ground and the contour lines are at integer intervals, i.e. tenfold increments in $P(\omega_l)$. The lowest contour line level (-9) was chosen to be just above the background-noise level before the onset of transition (see figure 9), so that the increase in power over a broad range of frequencies associated with the onset of transition is easily identifiable.

In all the plots in figure 18 there is a ridge centred on $\omega_l/\Omega = 1$, which is due to the small imbalance of the disk and can be disregarded. In figure 18(*a*), the ridge of high-amplitude spectral components at $R \approx 311$ clearly shows the broad range of frequencies excited by the pulsed disturbance (see also figure 12*b*). Immediately after initiation of the pulse, the large amount of energy present in the damped modes decreases and initially the growing modes are unable to compensate, resulting in a drop in disturbance amplitude and a decrease in bandwidth of the spectrum, which implies a spreading of the pulse in physical space. By the time the wave packet has moved to larger Reynolds numbers and $\theta_l = 20°$, the high-frequency components have decayed, while a peak has emerged for a range of ω_l/Ω centred on about 25. In figures 18(*c*) and 18(*d*), this peak begins to split into two separate peaks: a region that remains centred on $\omega_l/\Omega \approx 25$ and one centred on $\omega_l/\Omega \approx 10$. This could be an indication of the presence of two wave packets within the developing disturbance, as

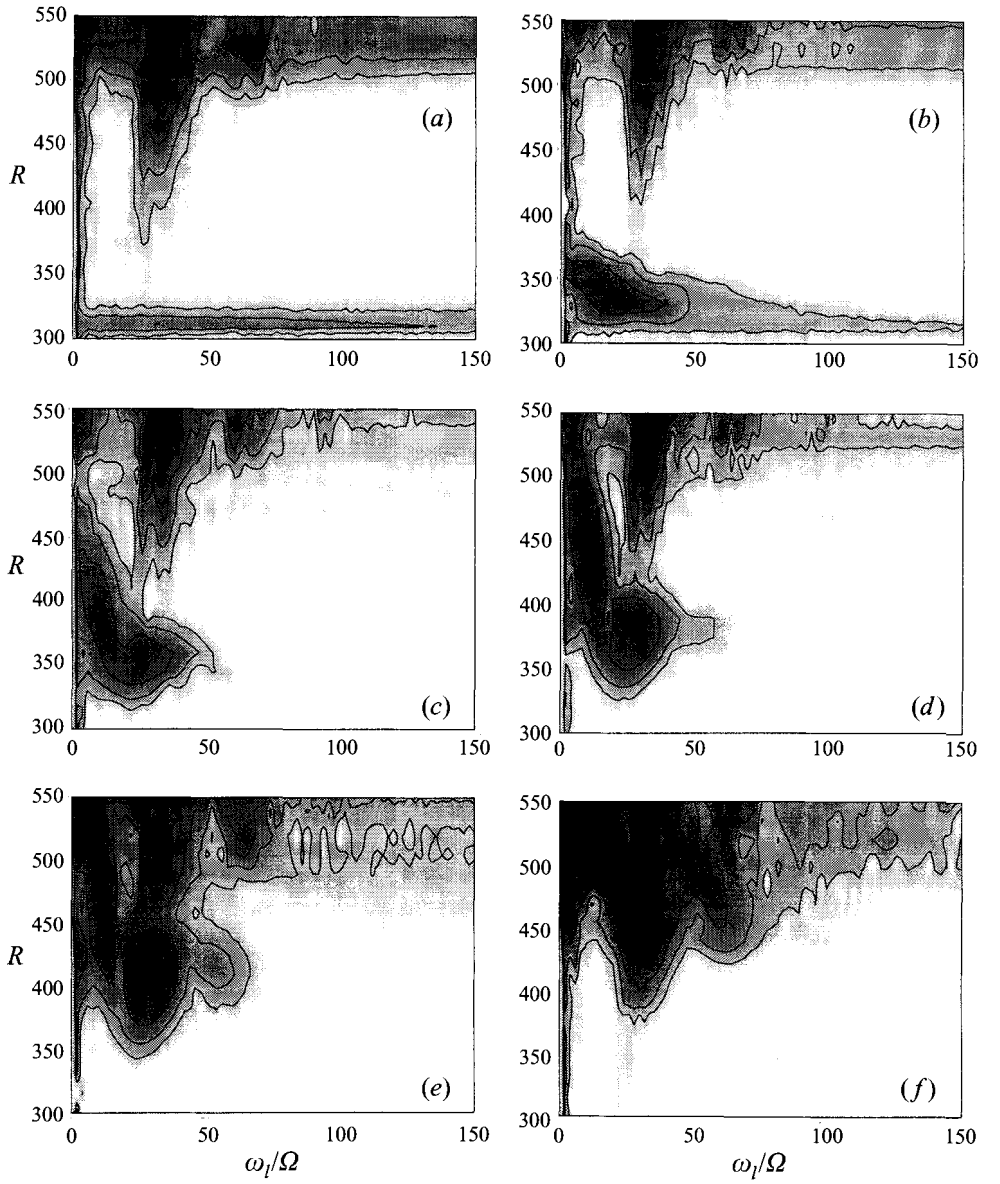

FIGURE 18. Contour plots of $\log(P(\omega_l))$ at $\Omega = 1400$ r.p.m. for the excited boundary layer: (*a*) $\theta_l = 0°$, (*b*) $\theta_l = 20°$, (*c*) $\theta_l = 40°$, (*d*) $\theta_l = 60°$, (*e*) $\theta_l = 80°$, (*f*) $\theta_l = 140°$. See figure 19 for the greyscale key.

expected from the fact that the dispersion relation supports two convectively unstable families of solution: branch-1 and branch-2 modes, both of which are discussed in §1. If this is the case, the higher-frequency peak is probably due to branch-2 instabilities, because it is dominant at low Reynolds numbers, and the lower-frequency peak is likely to be caused by branch-1 instabilities that become more dominant with increasing Reynolds number. The origins of these two peaks in $P(\omega_l)$ are discussed further in the next section, where time series are analysed using wavelet transforms.

The development of the peaks in $P(\omega_l)$ is complicated by their merger with contributions that are centred on $\omega_l/\Omega \approx 30$ for Reynolds numbers greater than

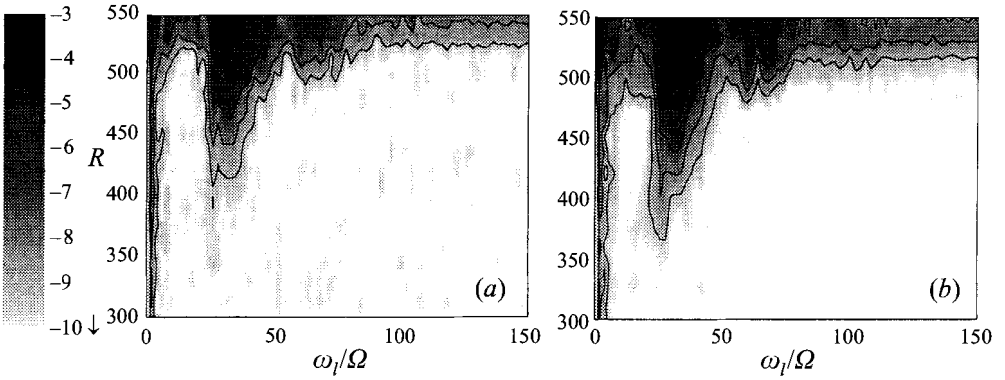

FIGURE 19. Contour plots of $\log(P(\omega_l))$ at $\Omega = 1400$ r.p.m. and $z = 1.3$: (*a*) $\theta_l = 330°$ for the excited boundary layer, (*b*) $\theta_l = 0°$ for the unexcited boundary layer.

about 400, which are probably due predominantly to stationary disturbances. Now that repeatable travelling waves have been excited, there is no guarantee that these components are due solely to stationary disturbances, only that the disturbances are deterministic. But the fact that, where they are distinct from the developing travelling frequency regions, they do not change much with θ_l suggests that approximately the same wave pattern is measured irrespective of the angular position of the probe, which is characteristic of disturbances that are fixed with respect to the disk. At higher θ_l, figure 18(*e*,*f*), the lower-frequency peak becomes less well defined and harmonics of the higher-frequency peak develop as it merges with the contributions centred on $\omega_l/\Omega \approx 30$. The background-noise level does not increase with the emergence of these harmonics, which suggests that although there must be some nonlinear behaviour it is does not yet promote the onset of transition. Spectra calculated from data measured at $\Omega = 1000$ r.p.m. are similar to those shown here, and all show that the broadband content characteristic of the onset of transition begins between $R \approx 500$ and $R \approx 520$; some of the variation in this threshold could be due to the fact that the ensemble-averaging process tends to increase the signal-to-noise ratio, making the spectra of ensemble-averaged time series less sensitive to emerging bursts of turbulence.

Beyond $\theta_l \approx 200°$ the qualitative features of the spectra do not change significantly: these spectra will be referred to as 'developed' spectra. Figures 19(*a*) and 19(*b*) show power spectra, plotted in the same way as figure 18, calculated from ensemble-averaged time series measured in the excited and unexcited boundary layer, respectively, where figure 19(*a*) is a developed spectrum measured at $\theta_l \approx 330°$. The agreement between the two figures suggests that the same behaviour occurs whether the boundary layer is externally excited or not, which is consistent with absolute instability promoting the onset of transition, because this mechanism can start from the smallest amount of noise and would operate even if appropriate frequencies were not artificially applied to the boundary layer. Note that in a convective flow, such as the Blasius boundary layer, the introduction of artificial disturbances dramatically changes the Reynolds number at which transition is observed.

3.3.3. *Wavelet-transform analysis*

In contrast to a Fourier-transform analysis, a wavelet-transform analysis can be used to decompose a signal into frequencies that are localized in time. Thus, this method can be used to associate certain frequency components revealed by the power spectra in the previous section with particular features in the time series.

Farge (1992) has recently reviewed the use of wavelet transforms in fluid mechanics. A time series $f(t)$ can be decomposed into a set of wavelet coefficients $W(t_o, s)$, where s is a parameter that characterizes a scale, or frequency, in the signal and t_o is a point in the time series. The magnitude of a wavelet coefficient gives a measure of the energy in the signal at a particular point in the time series of a particular frequency. A wavelet transform $g(t;s)$, for fixed s, is chosen to have a simple structure, to be localized in space and scale and to have finite amplitude over a period of $O(s^{-1})$. A commonly used wavelet is the Morlet wavelet (cf. equation (23) of Farge 1992), which is given by

$$g(t;s) = \mathrm{e}^{-(st)^2/2 - \mathrm{i}mst}. \tag{3.2}$$

This wavelet is an oscillation with a Gaussian modulation and so resembles a wave packet. The parameter m determines the number of oscillations present in the wavelet; here m takes the value 5. For fixed s, the wavelet is translated by t_o and then projected onto the signal $f(t)$, giving

$$W(t_o, s) = s^{1/2} \int_{-\infty}^{\infty} f(t) g(t - t_o; s) \mathrm{d}t, \tag{3.3}$$

where the factor $s^{1/2}$ is used to normalize the energies in each scale. The expression (3.3) is evaluated most efficiently by taking the Fourier transforms of f and g and performing a convolution in the frequency domain, such that

$$\hat{f}(\omega_l) = \int_{-\infty}^{\infty} f(t) \mathrm{e}^{-\mathrm{i}\omega_l t} \mathrm{d}t, \tag{3.4}$$

$$\hat{g}(\omega_l; s) = \int_{-\infty}^{\infty} g(t; s) \mathrm{e}^{-\mathrm{i}\omega_l t} \mathrm{d}t, \tag{3.5}$$

and

$$\hat{h}(\omega_l; s) = \hat{f}(\omega_l) \hat{g}(\omega_l; s), \tag{3.6}$$

so the inverse Fourier transform gives

$$W(t_o; s) = \frac{s^{1/2}}{2\pi} \int_{-\infty}^{\infty} \hat{h}(\omega_l; s) \mathrm{e}^{\mathrm{i}\omega_l t} \mathrm{d}\omega_l. \tag{3.7}$$

Figure 20 shows a selection of time series measured at $\Omega = 1000$ r.p.m. and $\theta_l = 60°$ (each lasting one time period, but with the origin shifted by a constant amount) and the associated wavelet transforms plotted in $(\omega_l/\Omega,\ t/T)$-space, which is equivalent to $(s/\Omega,\ t/T)$-space, calculated using a code provided by J. J. Healey. This value of θ_l was chosen because the wave packet is still separated from the transitional flow and because the power spectra show two frequency regions with large spectral amplitudes at this angular position (see figure 9 *d*). The power spectra show that the frequency region centred on $\omega_l/\Omega \approx 10$ appears at higher Reynolds numbers than the region centred on $\omega_l/\Omega \approx 25$, but at some Reynolds numbers there are sizeable contributions to the spectra from both frequency regions; the wavelet transform can associate these frequency contributions to particular features in the time series.

Figure 20 (*a*) suggests that, at this Reynolds number, the wave packet is composed predominantly of a single convectively unstable family (branch 2) with frequencies centred on $\omega_l/\Omega \approx 25$. In figure 20 (*b*) at $R \approx 319$, a second family (branch 1) of unstable frequencies appears, centred on $\omega_l/\Omega \approx 10$ at a slightly earlier time. This family continues to grow in amplitude in preference to the first, which is no longer

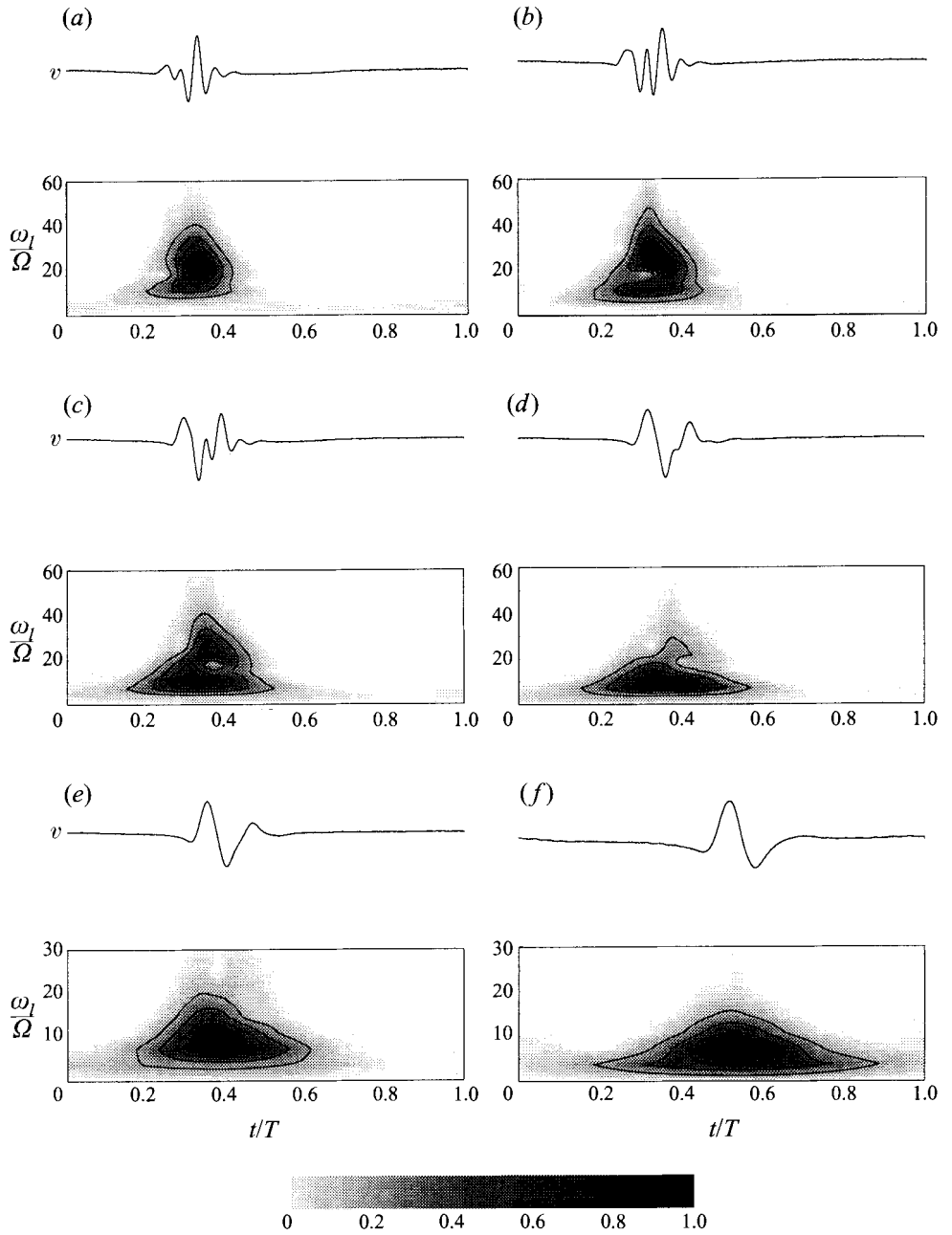

FIGURE 20. Peak-normalized ensemble-averaged time series, at $z = 1.3$, $\theta_l = 60°$ and $\Omega = 1000$ r.p.m. for the excited boundary layer, and associated wavelet transforms, in which the peak-normalized modulus of the wavelet coefficient is plotted: (*a*) $R \approx 306$, (*b*) $R \approx 319$, (*c*) $R \approx 333$, (*d*) $R \approx 346$, (*e*) $R \approx 359$, (*f*) $R \approx 413$. Note that the maximum frequency of (*e*) and (*f*) is half that of (*a–d*).

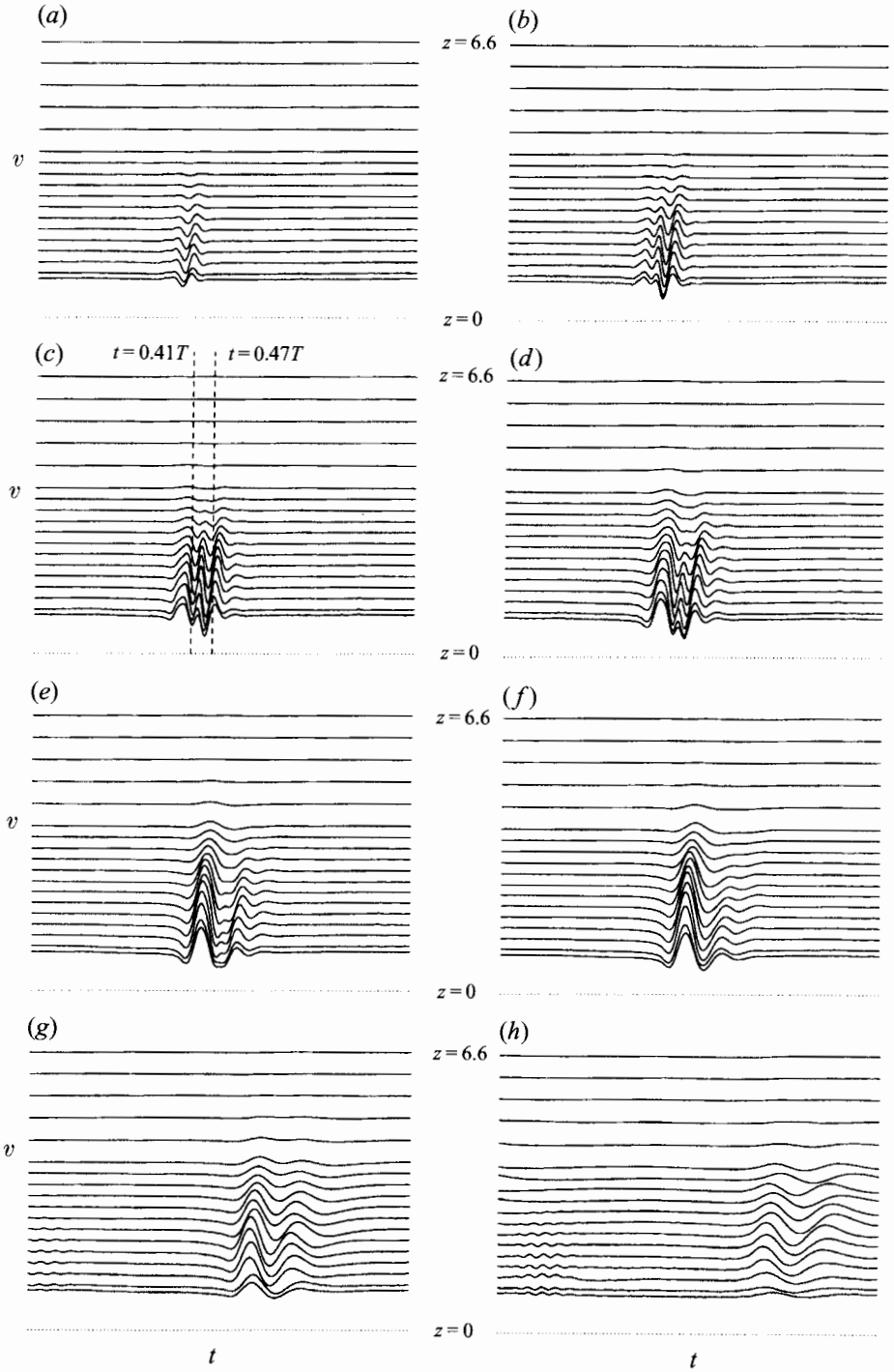

FIGURE 21. Ensemble-averaged time series of v for the excited boundary layer for $\theta_l = 50°$ and $\Omega = 1000$ r.p.m: (*a*) $R \approx 291$, (*b*) $R \approx 305$, (*c*) $R \approx 317$, (*d*) $R \approx 331$, (*e*) $R \approx 345$, (*f*) $R \approx 358$, (*g*) $R \approx 382$, (*h*) $R \approx 408$.

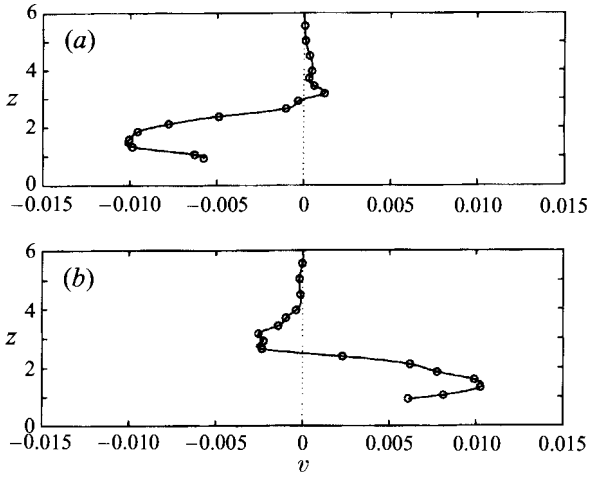

FIGURE 22. Instantaneous perturbation profiles taken from the ensemble-averaged time series measured at $R \approx 317$ for the excited boundary layer (figure 21 *c*): (*a*) $t/T \approx 0.41$, (*b*) $t/T \approx 0.47$.

detected at $R \approx 359$. Where both families are present, the wavelet transforms show that both are associated with the main wave packet and that they overlap in the time series. The lower-frequency peak corresponds to a point in the time series in front of that corresponding to the higher-frequency peak, implying that the former component of the wave packet lies at higher values of θ_l than the latter at fixed time.

3.3.4. *The axial structure of the excited disturbance field*

Here, the structure of the wave packet through the boundary layer is described. Figure 21 shows sets of ensemble-averaged time series of v, each lasting one time period, measured at $\Omega = 1000$ r.p.m, $\theta_l = 50°$ and a range of Reynolds numbers between 291 and 408. The wave packet at this θ_l and these Reynolds numbers is well defined and separated from the transitional flow. In figure 21, the vertical placement of each time series is proportional to its z-position and all the plots are to the same scale. The perturbations decay at large z and there is only a small drift of the perturbations to larger t with increasing z. At Reynolds numbers between about 305 and 358, and in figures 21 (*d*) and 21 (*e*) particularly, there are kinks in the time series that are indicative of two superposed packets with different phases, i.e. branch-1 and branch-2 packets (see §3.3.3). At Reynolds numbers outside this range, the disturbances look more like single wave packets with decreasing frequency of oscillation with increasing Reynolds number, as the branch-1 instabilities begin to dominate.

Figure 22 shows two instantaneous perturbation profiles for $\theta_l = 50°$ and $\Omega = 1000$ r.p.m. taken from the time series measured at $R \approx 317$ at the times indicated by the dashed lines in figure 21 (*c*), i.e. at $t/T \approx 0.41$ and $t/T \approx 0.47$. The measured data points (○) have been interpolated with cubic-spline fits to produce an approximate curve of the perturbation profile. These profiles have a maximum amplitude of about 1% of the local disk speed at $z \approx 1.3$ and a smaller maximum at $z \approx 3.0$. The maximum disturbance amplitude at $\theta_l = 50°$, which occurs at $R \approx 358$, in figure 21 (*f*), is about 2% of the local disk speed, which gives a similarly small degree of mean-flow distortion to that shown in figure 11 (*b*) for the unexcited boundary-layer flow.

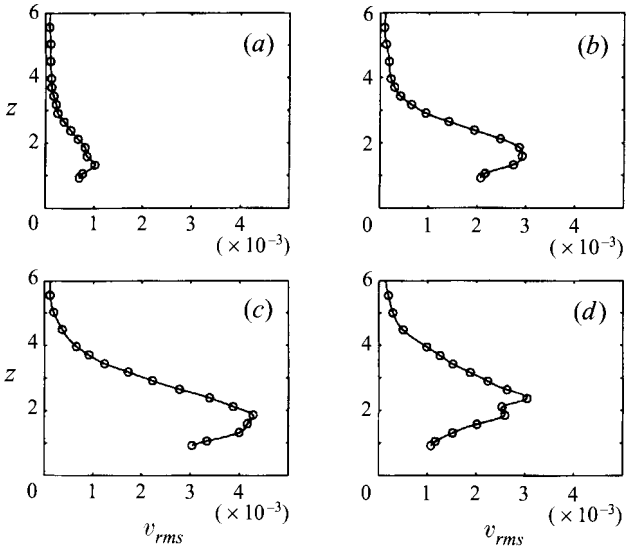

FIGURE 23. Profiles of v_{rms} for the excited boundary layer at $\theta_l = 50°$ and $\Omega = 1000$ r.p.m: (*a*) $R \approx 291$, (*b*) $R \approx 317$, (*c*) $R \approx 345$, (*d*) $R \approx 395$.

Because the instantaneous profiles change with time and with position it is difficult to provide a typical view; however, figure 23 characterizes the z-structure of the wave packet as it develops in space alone. The root-mean-square amplitudes of the circumferential velocity perturbations were calculated for the z-positions and Reynolds numbers depicted in figure 21 and example profiles of v_{rms} are plotted against z in figure 23. Again, the measured data points have been interpolated with cubic-spline fits to produce an approximate curve of the perturbation profile. At $R \approx 291$ the maximum is close to $z = 1.3$ but it tends towards $z = 2$ at higher Reynolds numbers. The maximum in figure 23 (*b*) is higher in the boundary layer than the maxima in figure 22 (both figures correspond to the same Reynolds number and θ_l), which illustrates the fact that at times other than those pictured in figure 22 there is a variation in the height of the largest perturbations. The smaller maximum at $z \approx 3.0$ in figure 22 is cancelled by perturbations at other times, giving a smooth profile in this region in figure 23 (*b*).

The maximum in the profiles develops a turning point at $R \approx 395$, and several more with increasing Reynolds number. The jaggedness of the profile occurs before the flow is transitional; therefore it is probably due to the presence of both stationary and travelling waves, which can be seen in figures 21 (*g*) and 21 (*h*) where stationary waves, with higher frequency than the travelling waves, lie to the left of the time series.

4. Conclusions

The measured laminar circumferential and radial velocity profiles were found to closely match the theoretical von Kármán profiles and the circumferential profiles resemble fully turbulent profiles by $R \approx 615$.

A study of the unexcited boundary-layer behaviour at two different disk speeds shows the disturbance field generated by unavoidable fixed roughness elements. The small hole through the disk creates a stationary wave pattern at the higher disk speed,

but at the lower disk speed there does not seem to be a pattern directly attributable to the hole. This difference could be due to the higher Reynolds number at the source or increased receptivity of the boundary layer to stationary perturbations at the higher disk speed. At least one other source of stationary disturbances, due to a surface imperfection, has been identified. Nonetheless, for both disk speeds, the stationary disturbances have a maximum amplitude of about 3% of the local disk speed at $R \approx 500$, which is less than a third of the threshold root-mean-square amplitude predicted by Balachandar *et al.* (1990) for the onset of secondary instabilities. A comparison with time series from Wilkinson & Malik (1985), which do show secondary instabilities, and a study of the instantaneous mean-flow distortion also suggest that the assumption made in Lingwood (1995*a*) that the linear stability of the flow is determined by the mean velocity profiles rather than secondary instabilities of modified profiles is justified. This will be true in general provided the stationary disturbance field is not too large. Merger of separate wave patterns with different phases from individual sources is characterized by a kink in the time series.

Analysis of ensemble-averaged and single-realization time series from the unexcited boundary-layer flow suggests that the onset of transition occurs at a Reynolds number above 502 and below 514. The transitional flow retains features from the laminar flow, but contains turbulent bursts that become more frequent with increasing Reynolds number. The convective region of the flow supports two families of travelling convectively unstable waves. The wave packet is formed predominantly from branch-2 modes close to its initiation but, with increasing Reynolds number and time, branch-1 modes grow preferentially until they dominate any branch-2 contributions. This behaviour is predicted by linear-stability theory. Where both families coexist, a wavelet-transform analysis shows that branch-1 contributions, which have about half the frequency, ω_l, of branch-2 modes, are centred slightly ahead of those of branch 2, but both types of disturbance overlap and propagate together as one wave packet.

Power spectra calculated from ensemble-averaged and single-realization time series from the unexcited boundary-layer flow show that the stationary disturbances have a spread of frequencies in the laboratory reference frame centred on about thirty times the disk rotation rate. This central frequency corresponds to thirty circumferential wavelengths in the rotating frame, which is consistent with the number of stripes observed in visualization experiments (e.g. Gregory *et al.* 1955). Above the critical Reynolds number for the onset of absolute instability, the power spectra from the excited flow (and single-realization power spectra from the unexcited flow) should include components due the absolute growth of certain waves but unfortunately the absolute frequencies coincide with the first harmonic of the stationary disturbances and the spectra do not show a well-defined absolute frequency ensuing close to the critical Reynolds number for the onset of absolute instability.

Nonetheless, more direct evidence that the flow becomes absolutely unstable is given by figure 15, which shows the progression of the wave packet in the radial direction with increasing time. This figure shows that the radial propagation of the trailing edge of the wave packet tends towards zero as the packet approaches the critical Reynolds number for the onset of absolute instability, causing an accumulation of energy at this Reynolds number or radius. The well-defined structure of the wave packet disintegrates when it reaches this Reynolds number. Power spectra from the excited flow at angular positions where the wave packet has merged with the transitional flow (termed developed spectra here) are similar to those from the unexcited flow, which suggests that the final state reached by the boundary layer is the same whether or not travelling waves are externally excited. This characteristic is consistent with

an absolute instability causing the onset of transition from laminar to turbulent flow, because above the critical Reynolds number the absolute instability can start from noise to reach the same final state, determined by nonlinear effects, as the boundary layer into which disturbances of appropriate frequency have been artificially added, giving a transition Reynolds number that is insensitive to changes in the exact form of the disturbance environment.

This work was supported by the Engineering and Physical Sciences Research Council, the Royal Society and the Boeing Commercial Airplane Group and was completed while supported by a Research Fellowship at Pembroke College, Cambridge.

REFERENCES

BALACHANDAR, S., STREETT, C. L. & MALIK, M. R. 1990 Secondary instability in rotating disk flow. *AIAA Paper* 90–1527.

BALAKUMAR, P. & MALIK, M. R. 1990 Traveling disturbances in rotating-disk flow. *Theor. Comput. Fluid Dyn.* **2**, 125–137.

BASSOM, A. P. & GAJJAR, J. S. B. 1988 Non-stationary cross-flow vortices in three-dimensional boundary-layer flows. *Proc. R. Soc. Lond.* A **417**, 179–212.

BASSOM, A. P. & HALL, P. 1991 Concerning the interaction of non-stationary crossflow vortices in a three-dimensional boundary layer. *Q. J. Mech. Appl. Maths* **44**, 147–172.

BRIGGS, R. J. 1964 *Electron-Stream Interaction with Plasmas*, chap. 2. MIT Press.

CHIN, D. & LITT, M. 1972 An electrochemical study of flow instability on a rotating disk. *J. Fluid Mech.* **54**, 613–625.

FALLER, A. J. 1991 Instability and transition of the disturbed flow over a rotating disk. *J. Fluid Mech.* **230**, 245–269.

FARGE, M. 1992 Wavelet transforms and their applications to turbulence. *Ann. Rev. Fluid Mech.* **24**, 395–457.

FEDOROV, B. I., PLAVNIK, G. Z., PROKHOROV, I. V. & ZHUKHOVITSKII, L. G. 1976 Transitional flow conditions on a rotating disk. *J. Engng Phys.* **31**, 1448–1453.

GASTER, M. & GRANT, L. 1975 An experimental investigation of the formation and development of a wave packet in a laminar boundary layer. *Proc. R. Soc. Lond.* A **347**, 253–269.

GRAY, W. E. 1952 The nature of the boundary layer at the nose of a swept back wing. Unpublished, Min. Aviation, London.

GREGORY, N., STUART, J. T. & WALKER, W. S. 1955 On the stability of three-dimensional boundary layers with application to the flow due to a rotating disk. *Phil. Trans. R. Soc. Lond.* A **248**, 155–199.

HEALEY, J. J. 1995 A new boundary layer resonance enhanced by wave modulation: theory and experiment *J. Fluid Mech.* **304**, 231–262.

HUERRE, P. & MONKEWITZ, P. A. 1985 Absolute and convective instabilities in free shear layers. *J. Fluid Mech.* **159**, 151–168.

HUERRE, P. & MONKEWITZ, P. A. 1990 Local and global instabilities in spatially developing flows. *Ann. Rev. Fluid Mech.* **22**, 473–537.

JOHANSSON, A. V. & ALFREDSSON, P. H. 1982 On the structure of turbulent channel flow. *J. Fluid Mech.* **122**, 295–314.

KÁRMÁN, TH. VON 1921 Über laminare und turbulente Reibung. *Z. Angew. Math. Mech.* **1**, 233–252.

KLINGMANN, B. G. B., BOIKO, A. V., WESTIN, K. J. A., KOZLOV, V. V. & ALFREDSSON, P. H. 1993 Experiments on the stability of Tollmien-Schlichting waves. *Eur. J. Mech.* B **12**, 493–514.

KOBAYASHI, R., KOHAMA, Y. & TAKAMADATE, CH. 1980 Spiral vortices in boundary layer transition regime on a rotating disk. *Acta Mech.* **35**, 71–82.

KOCH, W. 1985 Local instability characteristics and frequency determination of self excited wake flows. *J. Sound Vib.* **99**, 53–83.

KOHAMA, Y. 1984 Study on boundary layer transition of a rotating disk. *Acta Mech.* **50**, 193–199.

KOHAMA, Y. 1987 Crossflow instability in rotating disk boundary layer. *AIAA Paper* 87–1340.

LE GAL, P. 1992 Complex demodulation applied to the transition to turbulence of the flow over a rotating disk. *Phys. Fluids* A **4**, 2523–2528.

LINGWOOD, R. J. 1995*a* Absolute instability of the boundary layer on a rotating disk. *J. Fluid Mech.* **299**, 17–33.

LINGWOOD, R. J. 1995*b* Stability and transition of the boundary layer on a rotating disk. PhD thesis, Cambridge University.

MACK, L. M. 1985 The wave pattern produced by point source on a rotating disk. *AIAA Paper* 85–0490.

MACKERRELL, S. 1987 A nonlinear, asymptotic investigation of the stationary modes of instability of the three-dimensional boundary layer on a rotating disc. *Proc. R. Soc. Lond.* A **413**, 497–513.

MALIK, M. R., WILKINSON, S. P. & ORSZAG, S. A. 1981 Instability and transition in rotating disk flow. *AIAA J.* **19**, 1131–1138.

POLL, D. I. A. 1985 Some observations of the transition process on the windward face of a long yawed cylinder *J. Fluid Mech.* **150**, 329–356.

SHAIKH, F. N. 1993 Turbulent spots in a transitional boundary layer. PhD Thesis, Cambridge University.

SMITH, N. H. 1946 Exploratory investigation of the laminar-boundary-layer oscillations on a rotating disk. *NACA TN* 1227.

THEODORSEN, T. & REGIER, A. 1945 Experiments on drag of revolving disks, cylinders, and streamline rods at high speeds. *NACA Rep.* 793.

WILKINSON, S. P., BLANCHARD, A. E., GASTER, M., TRITZ, T., GAD-EL-HAK, M. & SELBY, G. 1989 Flow visualization of a wave packet on a rotating disk. In *Instability and Transition 1* (ed. Hussaini, M. Y. & Voigt, R. G.), pp. 306–318. Springer.

WILKINSON, S. P. & MALIK, M. R. 1985 Stability experiments in the flow over a rotating disk. *AIAA J.* **23**, 588–595.